Monthly Notices
of the
ROYAL ASTRONOMICAL SOCIETY

MNRAS **462,** 190–205 (2016)
Advance Access publication 2016 July 13

doi:10.1093/mnras/stw1679

Supermassive black holes in the EAGLE Universe. Revealing the observables of their growth

Yetli Rosas-Guevara,[1,2★] Richard G. Bower,[2★] Joop Schaye,[3] Stuart McAlpine,[2] Claudio Dalla Vecchia,[4,5] Carlos S. Frenk,[2] Matthieu Schaller[2] and Tom Theuns[2]

[1]*DAS, University of Chile, Camino del Observatorio 1515, Las Condes, Santiago, Chile*
[2]*ICC, Physics Department, University of Durham, South Road, Durham DH1 3LE, UK*
[3]*Leiden Observatory, Leiden University, PO Box 9513, NL-2300 RA Leiden, the Netherlands*
[4]*Instituto de Astrofísica de Canarias, C/ Vía Láctea s/n, E-38205 La Laguna, Tenerife, Spain*
[5]*Departamento de Astrofísica, Universidad de La Laguna, Av. del Astrofísico Francisco Sánchez s/n, E-38206 La Laguna, Tenerife, Spain*

Accepted 2016 July 8. Received 2016 July 8; in original form 2016 March 30

ABSTRACT

We investigate the evolution of supermassive black holes in the 'Evolution and Assembly of GaLaxies and their Environments' (EAGLE) cosmological hydrodynamic simulations. The largest of the EAGLE volumes covers a $(100\,\mathrm{cMpc})^3$ and includes state-of-the-art physical models for star formation and black hole growth that depend only on local gas properties. We focus on the black hole mass function, Eddington ratio distribution and the implied duty cycle of nuclear activity. The simulation is broadly consistent with observational constraints on these quantities. In order to make a more direct comparison with observational data, we calculate the soft and hard X-ray luminosity functions of the active galactic nuclei (AGN). Between redshifts 0 and 1, the simulation is in agreement with data. At higher redshifts, the simulation tends to underpredict the luminosities of the brightest observed AGN. This may be due to the limited volume of the simulation, or a fundamental deficiency of the underlying model. It seems unlikely that additional unresolved variability can account for this difference. The simulation shows a similar 'downsizing' of the AGN population as seen in observational surveys.

Key words: black hole physics – methods: numerical – galaxies: active – galaxies: formation – quasars: general.

1 INTRODUCTION

Accreting supermassive black holes (SMBHs) are one of the most efficient sources of radiation in the Universe. During periods of strong activity, they are often prominent as optical nuclei of galaxies, and referred to as active galactic nuclei (AGN). From a theoretical perspective, the vast energy outputs of AGN offer an appealing explanation for the steep cut-off of the massive end of the galaxy luminosity function (e.g. Bower et al. 2006, Croton et al. 2006) and the scaling of the X-ray properties of galaxy groups and clusters (e.g. Binney & Tabor 1995; Churazov et al. 2001; McCarthy et al. 2010).

From an observational perspective, the strong correlation between the mass of the central SMBH and the properties of the host galaxy, such as its velocity dispersion and bulge mass (see review by Kormendy & Ho 2013, also by Graham 2016), is consistent with a causal connection. One way to explore this connection, is to examine the evolution of AGN, for example by constructing luminosity functions at different cosmic epochs. Integrating the total energy radiated over the AGN lifetime then provides a method of charting the build-up of the rest-mass energy of SMBHs (Soltan 1982).

Measurements of the luminosity distribution of AGN require large, unbiased samples selected over a wide range of redshifts and luminosities. Constructing such samples is difficult because a fraction of the emission that emerges from the SMBH is obscured by the surrounding gas and dust making an uncertain fraction of SMBH difficult to detect (Lansbury et al. 2015). Although spectroscopic optical surveys are able to scan wide areas and detect large numbers of AGN up to redshift $z = 6$, these surveys are biased to the brightest and most unobscured population of SMBHs. While the mid-infrared band can also be used to detect SMBHs via the reprocessed emission from dust heated by AGN activity, the emission from the SMBH is often overwhelmed by the host galaxy. X-rays therefore provide the most efficient and unbiased method of selection. Although soft X-rays are the most easily observed band, AGN selection is still biased due to gas extinction around the SMBH. This makes hard X-rays the least biased wavelength range to detect the full SMBH population as obscuration is greatly reduced. Recently, multiple large X-ray surveys have been carried out by Ueda et al. (2014),

★ E-mail: yrosas@das.uchile.cl (YR-G); r.g.bower@durham.ac.uk (RGB)

Aird et al. (2015) and Buchner et al. (2015). These studies have revealed that the AGN population evolves strongly and that their number density abruptly decreases between $z \approx (1–2)$ and today. Moreover, these studies show that there is strong 'downsizing' of the AGN population in the sense that the space density of higher-luminosity AGN peaks at higher redshifts.

Such deep X-ray surveys provide tests for models linking the build up of galaxies and their SMBHs. Recently, this has been explored using semi-analytic models where the growth of SMBHs and AGN feedback have been incorporated as analytic approximations. Typically, these models assume that AGN activity is triggered by major galaxy mergers or disc instabilities, and calibrate AGN feedback to reproduce the galaxy mass function (Bower et al. 2006; Croton et al. 2006; De Lucia & Blaizot 2007). After accounting for strong dust obscuration of faint AGN, such models have been able to reproduce the observed AGN luminosity functions and AGN downsizing (Fanidakis et al. 2012; Hirschmann et al. 2012). Such studies rely on summarizing complex hydrodynamic interactions by simple models, but provide important and useful approximations.

Hydrodynamic simulations offer an alternative approach, more clearly differentiating the resolved hydrodynamical interactions from the small-scale processes that cannot be directly resolved. AGN evolution has been explored by hydrodynamical simulations of isolated galaxy mergers (Springel, Di Matteo & Hernquist 2005) and small cosmological volumes at high redshift. In these simulations, SMBH growth and AGN feedback are incorporated as subgrid physics (Springel et al. 2005; Booth & Schaye 2009). SMBH accretion is typically based on the pure Bondi–Hoyle model (Bondi & Hoyle 1944) or on simple modifications of this (Springel et al. 2005; Booth & Schaye 2009). Recent studies, however, have recognized the importance of accounting for the effects of accreting high angular momentum material (e.g. Hopkins et al. 2009; Rosas-Guevara et al. 2015; Angles-Alcazar et al. 2016).

In addition, a fraction of the rest-mass energy of the accretion flow may be injected in the surrounding gas as thermal energy or a momentum driven wind or jet. Since such processes cannot be directly resolved, simulations choose to implement feedback in different ways, for example as thermal heating proportional to the mass accretion rate (e.g. Springel et al. 2005; Booth & Schaye 2009), by explicitly distinguishing quasar and radio modes (e.g. Sijacki et al. 2007; Vogelsberger et al. 2014), or by injection of momentum into the surrounding gas (e.g. Power, Nayakshin & King 2011; Choi et al. 2014).

The latest generation of cosmological hydrodynamic simulations can now track the evolution of a galaxy population resolving the formation of individual galaxies with a resolution of $\sim$700 pc within large cosmological volumes, typically 100 cMpc on a side (Vogelsberger et al. 2014; Khandai et al. 2015; Schaye et al. 2015). In this paper we will focus on the Evolution and Assembly of GaLaxies and their Environments (EAGLE) simulations (Crain et al. 2015; Schaye et al. 2015). The EAGLE simulations reproduce many properties of galaxies, such as: the evolution of the galaxy mass functions (Furlong et al. 2015a), the evolution of galaxy sizes (Furlong et al. 2015b), the colour–magnitude diagram (Trayford et al. 2016) and the properties of molecular and atomic gas (Lagos et al. 2015; Bahé et al. 2016). Much of the success in reproducing the properties of the massive galaxies is due to the effects of AGN feedback (Crain et al. 2015). A key question is, therefore, whether the model reproduces the observables of SMBH evolution in a cosmological context. This test is almost entirely independent of the calibration procedure used to select model parameters, since the calibration procedure only considered the normalization of the correlation between the present-day SMBH mass and galaxy stellar mass (Schaye et al. 2015).

In this paper we present the evolution of SMBHs in the EAGLE simulations from $z = 11$ to 0. We compare the predicted X-ray observables in EAGLE to observational data from X-ray deep fields up to redshift 7. Such deep fields roughly correspond to the size of the largest EAGLE simulation, implying that we are restricted to densities of moderately luminous AGN. In Section 2, we briefly outline the relevant subgrid physics used in the EAGLE project and describe how we compute the intrinsic X-ray emission from AGN using empirical corrections for the bolometric luminosity and the obscured fraction. In Section 3, we present the results of the simulation. We summarize the properties of local SMBHs, such as their mass function in Section 3.1. The evolution of the black hole mass function, the Eddington ratio distribution plane and the black hole mass-halo mass relation are investigated in Section 3.2. In Section 3.3 we compare the evolution of the AGN luminosity function in X-ray bands with the most recent observational estimates. We show that AGN in EAGLE follow a similar downsizing trend to that seen in observational data. Finally in Section 4, we summarize and discuss our main results. Additional tests of simulation convergence and parameter dependencies are given in Appendix A and in Appendix B.

2 CODE AND SIMULATIONS

2.1 Code

In this study we use simulations from the EAGLE project.[1] This consists of a large number of cosmological simulations, with variations in parameters, galaxy formation subgrid models and numerical resolutions, as well as a large, $(100\text{cMpc})^3$ volume reference calculation. Full details of the EAGLE simulations can be found in Schaye et al. (2015) and Crain et al. (2015) (hereafter S15 and C15); here we give only a brief overview.

The EAGLE simulations were performed with a modified version of the parallel hydrodynamic code GADGET-3 which is a computationally efficient version of the public code GADGET-2 (Springel 2005). The improvements to the hydrodynamics solver, which are collectively referred to as Anarchy, aim to better model hydrodynamical instabilities, as described in Dalla Vecchia (in preparation) (see also S15 and Schaller et al. 2015). Here, we concentrate on the reference model denoted as, Ref-L100N1504, which corresponds to a cubic volume of $L = 100$ comoving Mpc (cMpc) on a side. Initially, it employs 2×1504^3 particles. In order to study numerical *weak* convergence, we also use the simulations AGNdT9-L050N0752 and Recal-L025N0752 with box sizes $L = 50$ and 25 cMpc respectively, containing 2×752^3 particles per simulation. Numerical *weak* convergence is defined in S15 and reflects the need of recalibrating the subgrid parameters to model more faithfully the physical processes at increasing resolution. Further simulation variations are considered in Appendix A.

The EAGLE simulations start from cosmological initial conditions at $z = 127$. The transfer function for the linear matter power spectrum was generated with CAMB (Lewis, Challinor & Lasenby 2000), adopting the Planck Cosmology parameters (Planck collaboration I et al. 2014). The Gaussian initial conditions were generated using the linear matter power spectrum and the random phases from the public multiscale white noise Panphasia field (Jenkins 2013).

[1] http://eaglesim.org; http://eagle.strw.leidenuniv.nl

Table 1. Box length, initial particle number, initial baryonic and dark matter particle mass, comoving and maximum proper gravitational softening for the EAGLE simulations used in this paper.

Name	L [cMpc]	N	m_g [$M_\odot$]	m_{DM} [$M_\odot$]	ϵ_{com} [ckpc]	ϵ_{prop} [pkpc]
Ref-L100N1504	100	2×1504^3	1.81×10^6	9.70×10^6	2.66	0.70
AGNdT9-L050N0752	50	2×752^3	1.81×10^6	9.70×10^6	2.66	0.70
Recal-L025N0752	25	2×752^3	2.26×10^5	1.21×10^6	1.33	0.35

Table 2. Values of parameters that differ between the simulations. These parameters affects the subgrid physics from star formation and from black holes used in this work; $n_{H,0}$ y n_n affect the fraction of the available energy injected from SN II into the ISM (see S15); C_{visc} and ΔT_{AGN} affect the BH accretion rates and the energy released from AGN as indicated in the text.

Simulation prefix	$n_{H,0}$ [cm^{-3}]	n_n	C_{visc}	ΔT_{AGN} [K]
Ref	0.67	2/ln 10	2π	$10^{8.5}$
AGNdT9	0.67	2/ln 10	$2\pi \times 10^2$	10^9
Recal	0.25	1/ln 10	$2\pi \times 10^3$	10^9

Particle displacements and velocities are calculated using second-order perturbation theory (Jenkins 2010).

The setup of these simulations gives a mass resolution of $9.7 \times 10^6\,M_\odot$ for dark matter (and $1.81 \times 10^6\,M_\odot$ for baryonic) particles. The gravitational interaction between particles is calculated using a Plummer potential with a softening length of 2.66 comoving kpc limited to a maximum physical size of 0.70 kpc. The box sizes, particle numbers and mass and spaced resolutions are summarized in Table 1.

2.2 Subgrid physics

The galaxy formation subgrid physics included in these simulations is largely based on that used for the OWLS project (Schaye et al. 2010, see also Crain et al. 2009). Many improvements have been implemented, in particular in the modelling of stellar feedback and black hole growth. We provide a brief overview below. Further details can be found in S15 and an extensive comparison of the effects of varying the subgrid physics parameters is given in C15. The values of the parameters that differ between the simulations can be found in Table 2.

(i) *Radiative cooling and photoheating, star formation and stellar feedback.*
Radiative cooling and photoheating are as described in Wiersma et al. (2009a). The radiative rates are computed element by element in the presence of the cosmic microwave background (CMB) and the UV and X-ray background radiation from quasars and galaxies (model of Haardt & Madau. 2001). Eleven elements are tracked. The radiative cooling and heating rates are computed with the software Cloudy (Ferland et al. 2013). Prior to reionization, the gas is in collisional ionization equilibrium and no ionizing background is present.

Star formation is implemented following the model of Schaye & Dalla Vecchia (2008), including a metallicity dependent density threshold, $n_z^* \sim Z^{-0.64}$ (Schaye 2004) above which gas particles are allowed to form stars. The model parameters are chosen to reproduces the empirical Schmidt–Kennicutt law which is encoded in terms of a pressure law. A temperature floor is imposed as a function of density, $P \propto \rho^{\gamma_{eff}}$, for gas with $\gamma_{eff} = 4/3$. This value of γ_{eff} leads to the Jeans mass, and the ratio of the Jeans length to the SPH kernel length, being independent of density, avoiding spurious fragmentation due to a lack of resolution. Gas particles are stochastically selected for star formation and converted to collisionless star particles. Each star particle represents a simple stellar population formed with a Chabrier (2003) IMF.

Stellar evolution is implemented as described in S15 and Wiersma et al. (2009b). The stellar mass-loss and consequent metal enrichment of 11 elements are modelled via three channels: (1) AGB stars, (2) Supernova (SNe) type Ia and (3) Massive stars and core collapse SNe. The mass-loss of the stellar population, including metals, is added to the gas particles that are within an SPH kernel of the star particle.

Feedback from star formation is treated stochastically, using the thermal injection method described in Dalla Vecchia & Schaye (2012). The total energy available to inject into the ISM per core SN is assumed to be 10^{51} erg. This amount of energy is injected 30 Myr after the birth of the star particle. Neighbouring gas particles are selected to be heated stochastically based on the available energy, and then heated by a fixed temperature difference of $\Delta T = 10^{7.5}$K. The stochastic heating distributes the energy such that the cooling time relative to the sound crossing time across a resolution element allows the thermal energy to be converted to kinetic energy, limiting spurious losses. The fraction of the available energy injected into the ISM depends on the local gas metallicity and density.

(ii) *Black hole growth and AGN feedback.*
Haloes that become more massive than $1.48 \times 10^{10}\,M_\odot$ are seeded with black holes of $1.48 \times 10^5\,M_\odot$ ($1.48 \times 10^4\,M_\odot$ for the simulation Small-seeds-L050N0752 presented in Appendix A) using the method of Springel et al. (2005). In order to mimic dynamical friction, at each timestep the black holes less massive than 100 times the initial mass of the gas particles are relocated to the minimum of its local gravitational potential. SMBHs can then grow via gas accretion, where the accretion rates are calculated by the modified Bondi–Hoyle model presented in Rosas-Guevara et al. (2015):

$$\dot{M}_{accr} = \min\left(\dot{M}_{Bondi}\left[C_{visc}^{-1}(c_s/V_\Phi)^3\right], \dot{M}_{Bondi}\right), \quad (1)$$

where c_s is the sound speed, V_Φ is the SPH-average circular speed of the gas around the black hole and C_{visc} is a viscosity parameter that controls the degree of modulation of the Bondi–Hoyle rate, $\dot{M}_{Bondi}$, in high circulation flows. SMBH accretion rates are also Eddington limited. In contrast to Rosas-Guevara et al. (2015) and Booth & Schaye (2009), EAGLE accretion rates do not include an additional 'β-factor' to boost the accretion rates when the surrounding gas density is high. This parameter is largely degenerate with the C_{visc} parameter. The values of C_{visc} in the simulations are found in Table 2. SMBHs also grow via mergers when they are within their smoothing length and have sufficiently small radial velocity. Further details are given in S15. Following Springel et al. (2005), two masses are adopted for BH particles: a sub grid mass that is applied to the computation of the gas accretion rates and AGN feedback, and a particle mass that is used in the gravitational calculations. Initially,

the subgrid mass is smaller than the particle mass. Once the subgrid mass exceeds the particle mass, the SMBH accretes stochastically gas particles in its vicinity so both masses grow a step. This method ensures that subgrid masses can be smaller than particle mass whilst conserving the gravitating mass.

AGN feedback is implemented following the stochastic model of Booth & Schaye (2009). Thermal energy is injected into the surrounding gas as a fraction of the rest mass energy of the gas accreted by the SMBH. Neighbouring gas particles of the SMBH are stochastically selected and heated by a temperature difference of $\Delta T = 10^{8.5}$K for the simulation Ref-L100N1504 and 10^9K for the simulation AGNdT9-L050N0752. The scheme is similar to that used to implement feedback from star formation, but uses a significantly higher heating temperature for the energy injection events. It is important to emphasize the simplicity of the feedback scheme that we adopt: a single *mode* of AGN feedback is implemented throughout using a fixed efficiency of 0.1, from which, a fraction of 0.15 is coupled to the surrounding gas.

2.3 Simulation outputs

Most published papers by the EAGLE collaboration are based on the analysis of 29 'snapshot' outputs, containing the full information on all particles at a particular redshift. These provide a good census of the masses of SMBHs at one particular time. Since we are interested in the dominant black hole of each dark matter halo, we do not use the quantities tabulated in the public data base (McAlpine et al. 2016) as these correspond to summed quantities of all SMBHs within the halo. As discussed in that paper, these can differ significantly in the case of low-mass black holes.

Although 'snapshot' outputs can be used to construct the AGN luminosity function, the strong variability of AGN in the simulation means that the statistics of luminous AGN are poorly sampled. To obtain a better determination of the AGN luminosity functions, we make use of the more frequent 'snipshot' outputs. These are partial copies of the particle state of the simulation, which are output in order to track critical simulation quantities with higher time resolution. There are 406 (400, 406) 'snipshots' outputs for the Ref-L100N1504 (AGNdT9-L050N0752, Recal-L025N0752) simulation, with a temporal separation between 10 and 60 Myr. In the simulation, AGN are highly variable on significantly shorter time-scales, and we average the luminosity functions in ranges of snipshots in order to improve the statistical sampling of luminous outbursts. A detailed analysis of AGN variability will be presented in McAlpine et al. (in preparation). Although this procedure allows us to reduce sampling uncertainties due to variability, it does not allow us to include rare objects that are not present in the simulation volume. In Appendix A, we compare simulations with different volumes, but the same parameters. The analysis presented then suggests that variability is the dominant uncertainty and that the procedure we use does not appear to cause a significant underestimate of the abundance of luminous AGN.

To give an impression of the size of the SMBH population, the first SMBH appears in the Ref-L100N1504 simulation at $z = 14.5$, the most massive black hole has a mass of $M_{\rm BH} = 4.1 \times 10^9\,{\rm M}_\odot$ and is located in the most massive halo (which has a mass of $M_{200} = 6.4 \times 10^{14}\,{\rm M}_\odot$) at $z = 0$. The total number of SMBHs at $z = 0$ with mass larger than $10^6\,{\rm M}_\odot$ is 5627 of which 25 have masses $> 10^9\,{\rm M}_\odot$, 505 have masses $> 10^8\,{\rm M}_\odot$ and 1996 have masses $> 10^7\,{\rm M}_\odot$.

2.4 Post-processing and definition of accretion regimes

As we have previously stressed, the subgrid models of SMBH accretion and feedback used do not make any distinction between different regimes of SMBH accretion. *In post-processing,* we distinguish between the activity levels of SMBHs based on their Eddington ratio,

$$\lambda_{\rm Edd} \equiv \dot{M}_{\rm accr}/\dot{M}_{\rm Edd}, \tag{2}$$

where $\dot{M}_{\rm accr}$ and $\dot{M}_{\rm Edd}$ are the SMBH mass accretion rate and the Eddington limit respectively. We define two 'active' accretion regimes. For Eddington ratios larger than 10^{-2}, we assume that the nuclear disc around the SMBH is thin and radiative cooling is efficient. We therefore assume that the luminosity of the disc can be described by the standard Shakura–Sunyaev disc model (Shakura & Syunyaev 1973). Such sources will be highly luminous in X-rays. We will refer to SMBHs in this regime as *Shakura–Sunyaev discs* (SSDs). For $\lambda_{\rm Edd}$ in the range 10^{-4}–10^{-2}, we assume that the nuclear accretion disc is thick and radiatively inefficient. We will refer to these SMBH as *Advection Dominated Accretion Flows* (ADAFs) (Rees et al. 1982; Narayan & Yi 1994; Abramowicz, Chen & Taam 1995). By default, we assume that these sources make negligible contributions to the X-ray luminosity function. Such sources are, however, expected to dominate radio source counts. Finally, we classify those with $\lambda_{\rm Edd} < 10^{-4}$ as *inactive* and assume that such sources are essentially undetectable against the emission of the host galaxy.

Note that the choice of a threshold in the Eddington ratio to define both active states SSDs and ADAFs does not have a significant effect on the X-ray AGN luminosity functions as shown in Appendix B.

2.5 Predicting X-ray observables

In this section, we describe the method used to predict X-ray luminosities from the SMBH accretion rates. We consider only AGN in the SSD regime ($\lambda_{\rm Edd} > 10^{-2}$). For such sources, the bolometric luminosity is

$$L_{\rm bol} = \frac{\epsilon_{\rm r}}{1-\epsilon_{\rm r}}\dot{M}_{\rm BH}c^2 = \epsilon_{\rm r}\dot{\rm M}_{\rm accr}{\rm c}^2, \tag{3}$$

where $\epsilon_{\rm r}$ is the radiative efficiency and is set to 0.1 as suggested by Shakura & Syunyaev (1973).

We use the redshift independent bolometric corrections of Marconi et al. (2004) to convert the bolometric luminosity into intrinsic hard (2–10 keV) and soft (0.5–2 keV) X-ray band luminosities. The bolometric corrections are third degree polynomial relations defined as follows:

$$\log_{10}\left(\frac{L_{\rm HX}}{L_{\rm bol}}\right) = -1.54 - 0.24L - 0.012L^2 + 0.0015L^3$$

$$\log_{10}\left(\frac{L_{\rm SX}}{L_{\rm bol}}\right) = -1.64 - 0.22L - 0.012L^2 + 0.0015L^3, \tag{4}$$

where $L = \log_{10}(L_{\rm bol}/{\rm L}_\odot) - 12$. The bolometric corrections are computed with a template spectrum that is truncated at $\lambda > 1\,\mu$m to exclude the IR bump (Marconi et al. 2004) produced by reprocessed UV radiation. The correction is assumed to be independent of redshift. We note that Vasudevan & Fabian (2009) have suggested that the bolometric corrections may be a function of the Eddington ratio, but the differences are not significant except in AGN with $\lambda_{\rm Edd} < 10^{-2}$. Lusso et al. (2012) suggested that the bolometric corrections could be lower than those of Marconi et al. (2004) at high bolometric luminosities, but the offset is small in the context of this work.

Hopkins, Richards & Hernquist (2007) also proposed expressions for the bolometric corrections based on dust absorbed luminosities. For us, this is inappropriate since we base our analysis on intrinsic X-ray luminosities. Thus, we opt for the relations of Marconi et al. (2004) which has the benefit of being consistent with previous studies. Hereafter, we always refer to luminosity $L_{\rm HX}$ ($L_{\rm SX}$) as the intrinsic luminosity in the 2–10 kev (0.5–2 keV) rest-frame energy range.

The emission of AGN may be absorbed if the circumnuclear environment is rich in gas and dust. The absorption is likely to be highly anisotropic, making a fraction of sources undetectable in the soft X-ray band. From the observational data, it is unclear whether the obscured fraction is a function of redshift and other sample properties. For example, early studies (e.g. Ueda et al. 2003; Steffen et al. 2003) did not find clear evidence for a redshift dependence, but recent studies have established that the obscured AGN fraction increases with increasing redshift (e.g. Hasinger 2008; Treister, Urry & Virani 2009; Ueda et al. 2014). Because of these uncertainties, we prefer to compare the simulations to observed soft X-ray luminosity functions for which the obscured fraction has already been taken into account by simultaneously fitting to both hard and soft X-ray data (Aird et al. 2015). In future work, we will investigate the obscuration of AGN due to gas and dust, taking into account the properties of the host galaxy.

3 RESULTS

3.1 Properties of nearby SMBHs

The SMBH mass function provides a useful overview of the SMBH population at low redshift. To determine the average SMBH mass function with reduced sampling noise, we combine snipshot outputs as explained in Section 2.3. Fig. 1 shows the SMBH mass function for the Ref-L100N1504 (dark blue line), AGNdT9-L050N0752 (light blue line) and Recal-L025N0752 (green line) simulations. In order to facilitate comparison with later plots and observational data, we include only the central black hole of each galaxy. The level of agreement between simulations is good (better than 0.2 dex) for SMBHs with mass $> 10^6\,{\rm M}_\odot$. This level of agreement is encouraging, but note that the EAGLE simulations were calibrated to reproduce the normalization of $M_{\rm BH}$-$M_{\rm star}$ relation at $z = 0$ (see S15, fig. 10). It is interesting to note the similarity of the high-mass end of the Ref-L100N1504 and AGNdT9-L050N0752 simulations. Given the more effective AGN feedback in the AGNdT9-L050N0752 model, we might have expected a divergence at the massive end due to its greater gas mass-loss from galaxy groups. Clearly this is not the case. In Appendix A, we show that for SMBHs with mass $\lesssim 1.6 \times 10^6\,{\rm M}_\odot$ the mass function depends strongly on the seed black hole mass and we indicate this region by dotted lines.

It is interesting to compare the simulation SMBH mass functions to the estimates based on observational data. Because SMBH masses can be directly determined only in an incomplete sample of galaxies (Kelly & Shen 2013), it is important to note that the observational estimates of the SMBH mass function are indirect and must be inferred from the correlations between SMBHs and the properties of their host galaxy bulge. In the Fig. 1, we show estimate from Marconi et al. (2004) (grey circles), Shankar et al. (2004) (grey squares) and more recent data from Shankar (2013) (red and grey regions). Shankar (2013) and Shankar et al. (2004) use the $M_{\rm BH}$-σ correlation, while Marconi et al. (2004) use the relation between SMBH mass and bulge luminosity. The simulated SMBH mass function is in reasonable agreement with the observational estimates

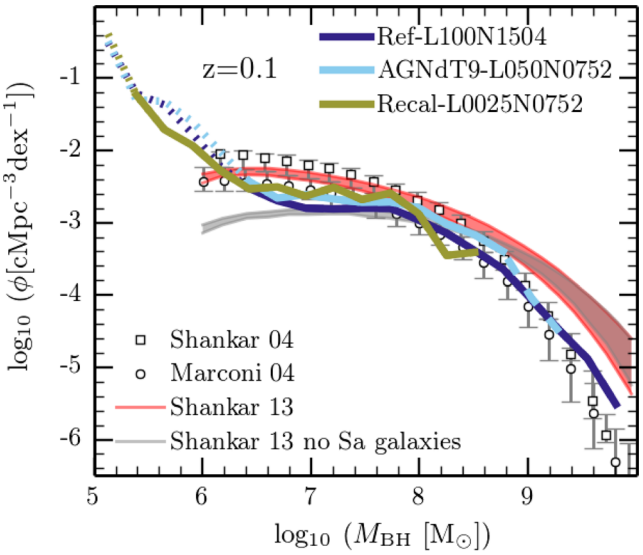

Figure 1. The SMBH mass functions of AGNdT9-L050N0752 (light-blue), Ref-L100N1504 (blue) and Recal-L025N0752 (green) at $z = 0.1$ The dotted part of each curve corresponds to SMBH masses below to the initial mass of a gas particle. The dashed part at the high-mass end indicates the SMBH mass bins containing fewer than 10 objects per mass bin. The grey region corresponds to the observational estimate of Shankar (2013) who uses the $M_{\rm BH} - \sigma$ relation from McConnell & Ma (2013), while the red region corresponds to an estimate in which the SMBHs in the centre of Sa type-galaxies are included. Older observational estimates from Marconi et al. (2004) and Shankar et al. (2004) are shown as data points. The observational estimates all infer the black hole mass function indirectly and the differences are primarily driven by the choice of the $M_{\rm BH}$-σ calibration.

from Shankar et al. (2004) and Marconi et al. (2004) over a wide mass range, but underestimates the abundance of the high-mass SMBHs when compared to Shankar (2013). This discrepancy is somewhat surprising since both the simulation and Shankar (2013) are calibrated to SMBH masses from McConnell & Ma (2013). The discrepancy, and the variance between observational estimates, illustrates the uncertainty in deriving the SMBH mass function from observational data. Indeed, Shankar (2013) note that adopting different variations of the SMBH scaling relations leads to large variations in the inferred SMBH mass function, since the scatter and mass range covered by the data must be taken into account. For example, Shankar (2013) show that the low-mass end of their mass function depends strongly on how the $M_{\rm BH}$-σ correlation is applied to galaxies of different morphological types. The red region assumes that the relation can be applied regardless of morphology, while the grey region assumes that Sa and late-type galaxies do not have an SMBH. Thus, although there are some differences between the simulated SMBH mass function and the more recent observational estimates, these depend heavily on how the observational calibration data is extrapolated. For this reason, it is far better to validate the simulation by comparing to the black hole mass-stellar mass relation directly and in Schaye et al. (2015) we show that the simulation reproduces the observational data within their uncertainties.

Integrating the mass function, we obtain the predicted black hole mass density at $z = 0.1$. In the Ref-L100N1504 simulation, we find it to be $2.6 \times 10^5\,{\rm M}_\odot{\rm Mpc}^{-3}$, closely matching the observational value estimated by Yu & Tremaine (2002) ($2.6 \pm 0.4 \times 10^5\,{\rm M}_\odot{\rm Mpc}^{-3}$, adjusted to Planck Cosmology parameters), whose calculations are based on the velocity dispersion of early-types galaxies in the Sloan Digital Survey (SDSS). This

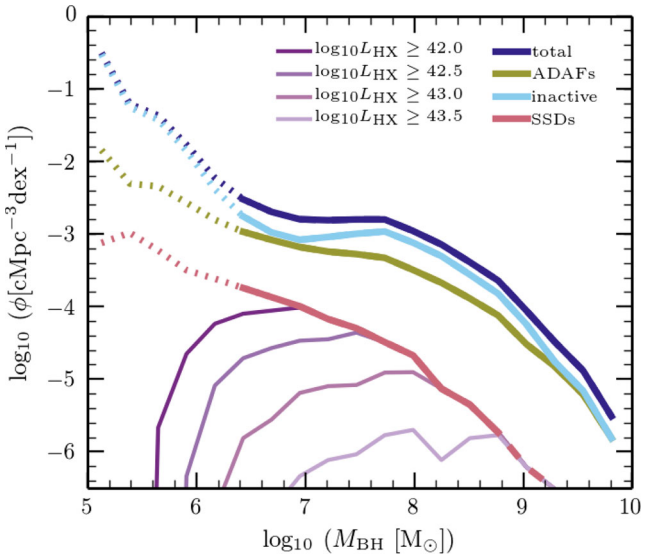

Figure 2. The contributions of different accretion regimes to the predicted SMBH mass function for the Ref-L100N1504 simulation at $z = 0.1$. The dotted part of each curve corresponds to masses smaller than the initial mass of a gas particle and the dashed part of the curve to mass bins containing fewer than 10 objects. The dark blue line is the total SMBH population, the light blue line corresponds to inactive SMBHs ($\lambda_{\rm Edd} < 10^{-4}$), the green line to SMBHs accreting as ADAFs ($10^{-4} \leq \lambda_{\rm Edd} < 0.01$) and the red line to SSDs ($\lambda_{\rm Edd} \geq 0.01$). Purple lines in the figure show the effect of also requiring the SSD sources to exceed a luminosity limit, as would be the case in an observational survey. The figure shows that inactive SMBH dominate the SMBH mass function over a wide mass ranges, with a negligible contribution to the most massive SMBHs ($>10^8\,{\rm M}_\odot$) from SSDs. Comparing the contributions of different accreting SMBHs to the total SMBH mass function, the average 'duty cycle' of SMBHs is determinated. The predicted duty cycle for SSDs is ∼0.01 in agreement with observational estimates.

value is also consistent with the result from Aird et al. (2010) who used hard X-ray luminosities to compute the total energy released by the SMBH population through time ($2.2 \pm 0.2 \times 10^5\,{\rm M}_\odot{\rm Mpc}^{-3}$), although is lower than the estimate of Marconi et al. (2004) ($4.6^{+1.9}_{-1.4} \times 10^5\,{\rm M}_\odot{\rm Mpc}^{-3}$).

In Fig. 2 we dissect the SMBH mass function according to accretion regime. We distinguish inactive SMBHs (light blue), ADAFs (green) and SSDs (red). The three SMBH populations differ greatly in normalization. Most SMBHs are inactive, corresponding to 70 per cent of the total SMBH population with $M_{\rm BH} > 10^7\,{\rm M}_\odot$, while ADAFs (green line) correspond to 29 per cent and SSDs correspond to only ∼1 per cent of the population. The figure shows results from the Ref-L100N1504 simulation, but the breakdown is similar in the other simulations. Since SMBHs frequently switch between states between output times, we can view the differences in normalization as an average *duty cycle*, and interpret the relative normalization of the mass functions as the probability of finding an SMBH in any given state.

The duty cycle, that is the fraction of the time an SMBH is active, shortens with increasing SMBH mass, with the probability of classifying an SMBH as an active SSD varying from 0.05 for $M_{\rm BH} \sim 10^6\,{\rm M}_\odot$ to 0.01 $M_{\rm BH} \sim 10^8\,{\rm M}_\odot$. At higher masses, the probability of finding a present-day SMBH in the SSD state becomes extremely small. Restricting the comparison to the SMBH population with $M_{\rm BH} > 10^7\,{\rm M}_\odot$, the SSD fraction is 0.02 on average. This is consistent with the observational estimates of the average AGN lifetime for $M_{\rm BH} < 10^8\,{\rm M}_\odot$ that corresponds to $3-13 \times 10^7$ years (e.g. Yu & Tremaine 2002; Marconi et al. 2004).

These trends are not particularly sensitive to the choice of the threshold used to define SSD systems; however, an observational survey will only detect black holes that exceed an X-ray luminosity (or flux) limit. Purple lines in Fig. 2 show the effect this has on the fraction of black holes that are detectable in an ideal hard (2–10 keV) X-ray survey. Our estimates account for bolometric corrections (as described in Section 2.5) but do not account for additional selection effects, such as the difficulty of distinguishing faint AGN from emission associated with star formation. We focus on the results for an observational survey with a luminosity limit of $L_{\rm HX} > 10^{43}\,{\rm erg\,s}^{-1}$. For the highest mass black holes, all the SSD systems are detected, but below a black hole mass of $10^8\,{\rm M}_\odot$, the observable population become increasingly biased. For black holes of mass $10^7\,{\rm M}_\odot$, the detected population accounts for only 6 per cent of the SSD population and 0.3 per cent of all black holes of that mass. As black hole masses drop below $10^6\,{\rm M}_\odot$, the population becomes undetectable because of the Eddington limit. Fortunately, in practice, observational surveys are flux limited so that a range of luminosity limits can be probed; nevertheless, this exercise highlights the difficulty of constructing a complete census of the black hole population. We examine the X-ray emission of the simulation's black hole population in more detail in Section 3.3.1.

3.2 Properties of high-redshift SMBHs

Having examined the properties of SMBHs at low redshift, we now investigate the evolution of SMBHs. We will look at the evolution of the SMBH mass function, the $\lambda_{\rm Edd}$-$M_{\rm BH}$ distribution and the SMBH mass-halo mass relation.

3.2.1 The SMBH mass function

Fig. 3 investigates the evolution of the SMBH mass function. Between $z = 5.1$ and $z = 1.0$, the normalization of the SMBH mass function rapidly evolves by an order of magnitude. While the overall normalization changes little at lower redshifts ($z < 1$), the abundance of the most massive objects increases as the break in the mass function becomes shallower with cosmic time, and the dip seen at low masses at intermediate redshifts is filled in. The evolution of the SMBH mass function is similar to the evolution of the galaxy stellar mass function (see Furlong et al. 2015a, fig. 2).

In Fig. 4, we show the evolution of the different accretion regimes. The contributions of ADAFs (green lines), SSDs (red lines) and inactive SMBHs (light blue) evolve relative to each other. At $z < 2$ the abundance of the SMBH mass function is dominated by ADAFs and inactive SMBHs, preserving a similar shape to the total SMBH mass function. In contrast, the SSD population evolves rapidly in normalization from $z = 2$ to $z = 0.1$, also showing a rapid decrease in characteristic mass. This is a feature of AGN 'downsizing' which we will return in the following sections. At $z > 2$ the inactive SMBH population declines and the dominant populations are SSDs and ADAFs. The results described above show that there is switch in the nature of black hole accretion with cosmic time. Below $z = 2$, the population is dominated by inactive SMBHs or ADAFs and only a tiny fraction is undergoing strong accretion. At high redshift, SMBHs undergo much more frequent high Eddington-rate accretion events.

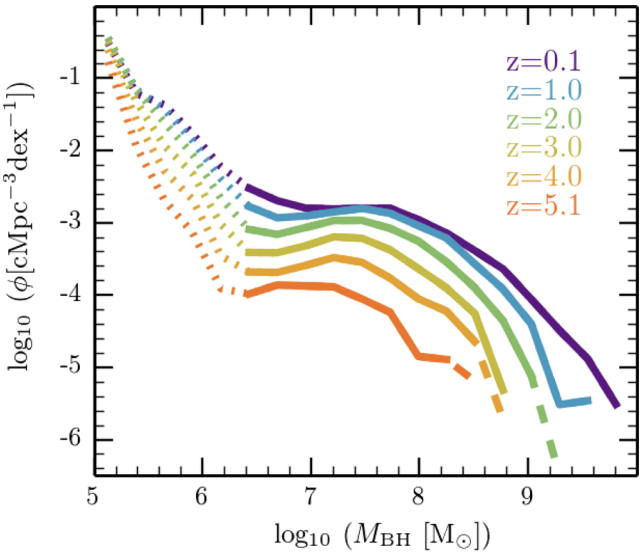

Figure 3. The evolution of the SMBH mass function from $z = 5.1$ to $z = 0.1$ in the Ref-L100N1504 simulation. The dotted part of the SMBH mass function corresponds to masses smaller than the initial mass of gas particles. The dashed part corresponds to mass bins containing fewer than 10 objects. Colours represent different redshifts as indicated in the legend. The SMBH mass function shows a rapid evolution in the normalization over the whole mass range from $z = 5.1$ to $z = 1$. Towards lower redshifts ($z < 1$), the evolution is mostly restricted to a flattening of the slope at the high-mass end.

3.2.2 *The* $\lambda_{\rm Edd}$-$M_{\rm BH}$ *plane*

In Fig. 5 we show Eddington ratio, $\lambda_{\rm Edd} = \dot{M}_{\rm BH}/\dot{M}_{\rm Edd}$, as a function of black hole mass in the Ref-L100N1504 simulation from redshifts 0–5. Overall, the median Eddington ratio decreases as a function of the black hole mass, with the SMBHs with mass 10^6–10^7 $M_\odot$ the most active population in the simulation through cosmic time. However, there is large scatter (∼2 dex) in the distribution of Eddington ratios for any given SMBH mass due to the high variability of the mass accretion rates.

For a given SMBH mass, the median value of $\lambda_{\rm Edd}$ moves towards lower values as redshift decreases. This trend is more evident in SMBHs with $M_{\rm BH} < 10^7$ $M_\odot$, where the median of $\log_{10}\lambda_{\rm Edd}$ declines from ~ -1 at $z = 3$ to -3 at $z = 0$. For SMBHs with higher mass, the median changes less dramatically, consistent with the difference in the evolution of the active and inactive SMBH populations shown in Fig. 4. The figure also highlights that SMBHs of mass $<10^7$ $M_\odot$ have an increasing tendency to be limited by the Eddington accretion rate at higher redshift, making it possible to build quasar-mass black holes early in the history of the Universe. In general, however, the SMBHs in the simulation accrete well below their Eddington limit.

3.2.3 *The* $M_{\rm BH}$-M_{200} *relation*

Fig. 6 shows the evolution of the central SMBH mass–halo mass relation for different redshifts from $z = 5$ to $z = 0$.

We also include the estimates at $z = 0$ from observations of strong gravitational lenses by Bandara, Crampton & Simard (2009) as grey diamonds and the grey line. In comparison to the simulations,

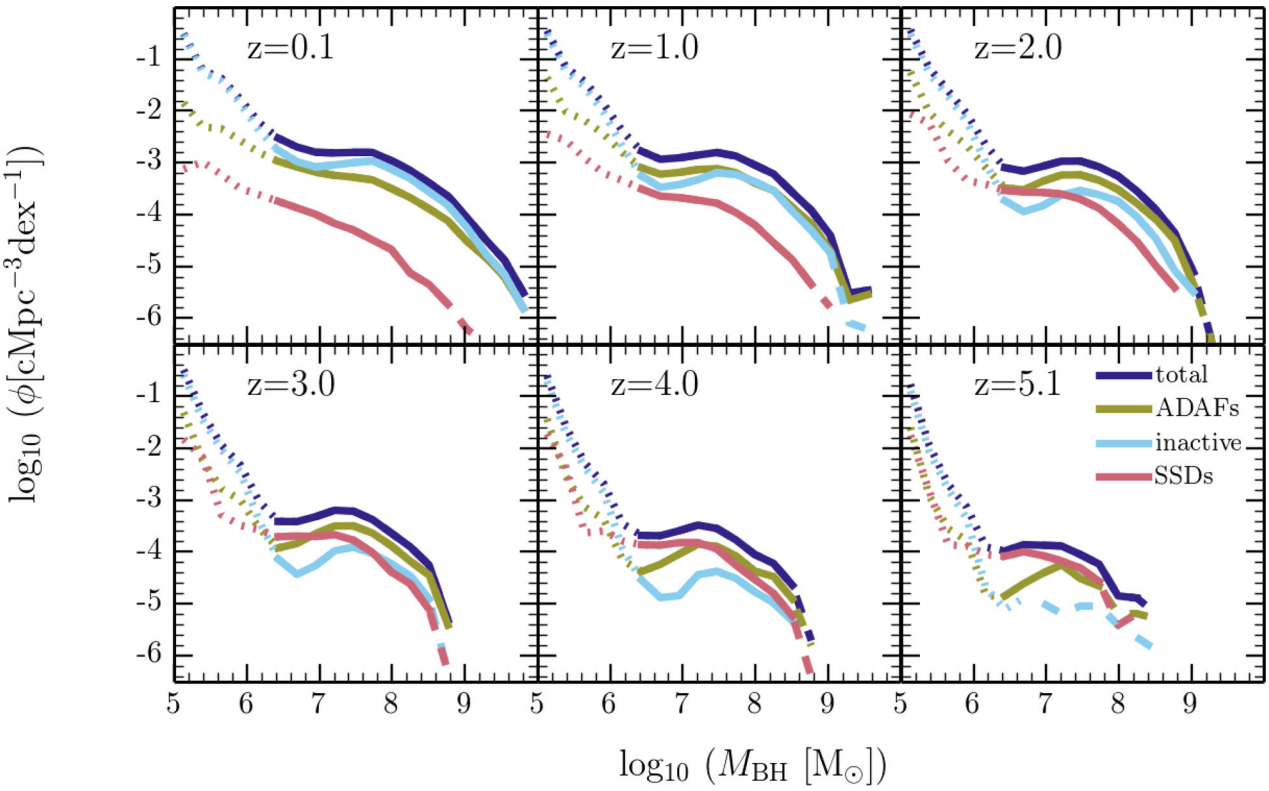

Figure 4. Evolution of the SMBH mass function split by accretion regime: light-blue lines correspond to inactive SMBHs ($\lambda_{\rm Edd} < 10^{-4}$), green lines to SMBHs accreting as ADAFs ($10^{-4} \leq \lambda_{\rm Edd} < 10^{-2}$) and red lines to SSDs ($\lambda_{\rm Edd} \geq 10^{-2}$) from $z = 0.1$ to $z = 5.1$. At low redshift, the mass function is dominated by the inactive and ADAFs population, whereas at high redshift, the SSDs and ADAFs are the most abundant.

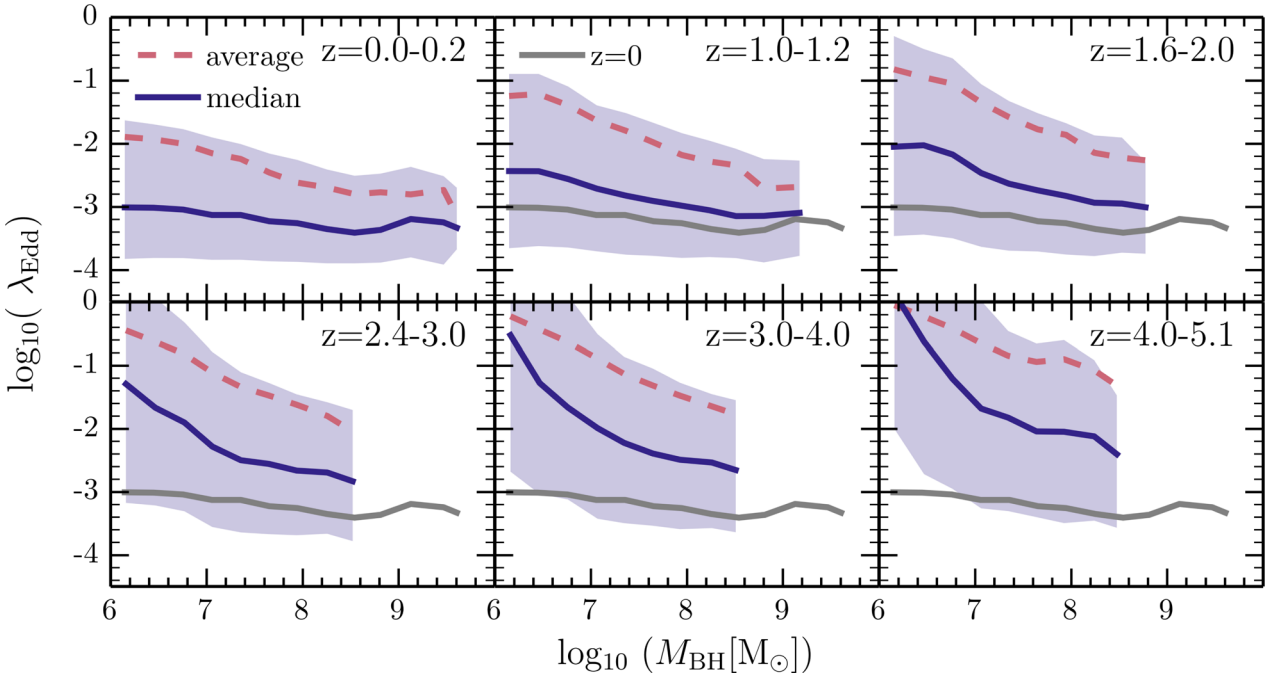

Figure 5. Evolution of the Eddington ratio distribution ($\lambda_{\rm Edd} = \dot{M}_{\rm BH}/\dot{M}_{\rm Edd}$), plotted as a function of black hole mass. Median and average $\lambda_{\rm Edd}$ are shown as solid blue and dashed pink lines, respectively. Only SMBHs with $M_{\rm BH} > 10^6\,{\rm M}_\odot$ are shown. The grey solid line repeats the median of the distribution at $z = 0$. The coloured region represents the 10th and 90th percentiles of the distribution. $\lambda_{\rm Edd}$ increases as redshift increases, particularly for lower mass black holes. SMBHs with $M_{\rm BH} \lesssim 10^7\,{\rm M}_\odot$ have an increasing tendency to be limited by the Eddington accretion rate at $z > 2$.

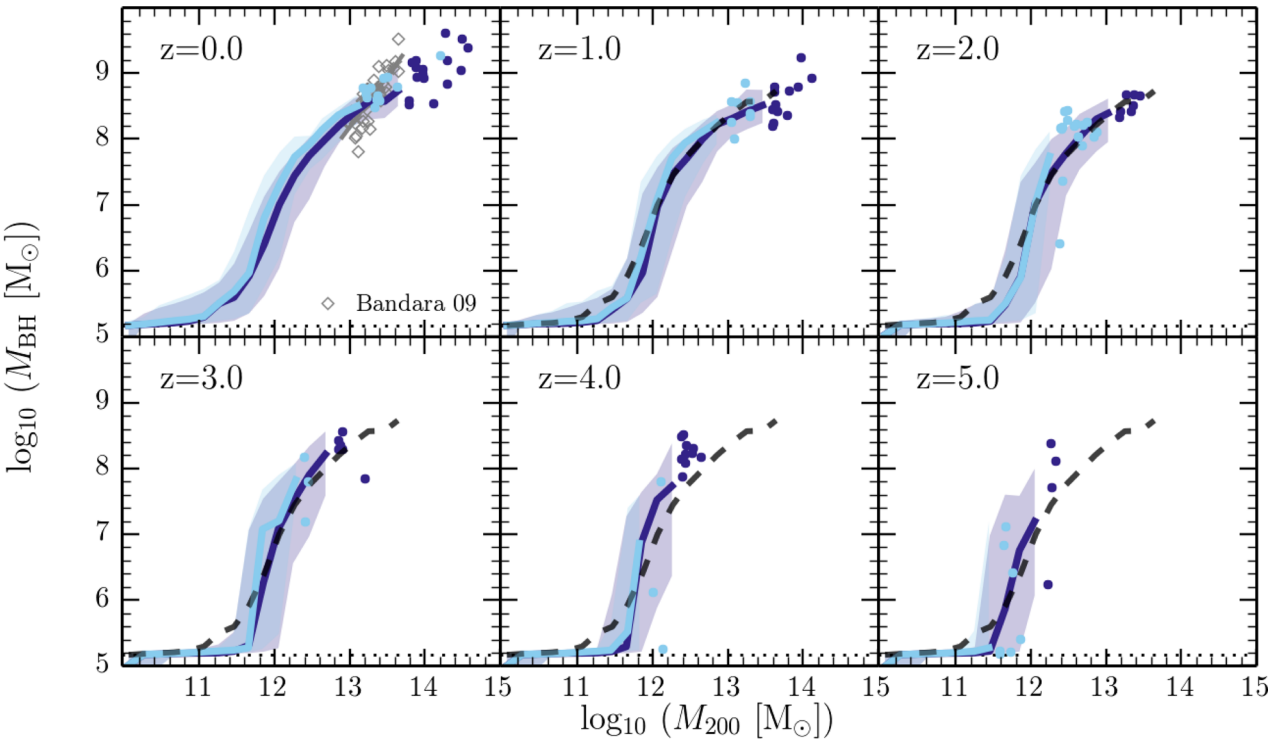

Figure 6. The $M_{\rm BH}$-M_{200} relation for various redshifts from $z = 0$ to $z = 5$. Solid lines represent the median for the simulations Ref-L100N1504 (dark blue) and AGNdT9-L050N0752 (light blue). Circles show individual haloes for bins with less than 10 haloes per dex mass bin. Coloured regions represent the 10th to 90th percentiles of the distribution, and the dark dashed line represents the $M_{\rm BH}$-M_{200} relation at $z = 0$. Grey diamonds show observational estimates from Bandara et al. (2009) and the grey solid line the fit to the $M_{\rm BH}$-M_{200} relation found in that paper. The dotted horizontal line shows the BH seed mass. The $M_{\rm BH}$-M_{200} relation undergoes a transition for haloes with $M_{200} \sim 10^{11.6}\,{\rm M}_\odot$. The transition evolves little with redshift, showing only a tendency to be slightly more abrupt at higher redshifts.

Bandara et al. (2009) find a steeper relation, but this calculation was based on the assumed form of the $M_{\rm BH}$-σ relation and not on direct observations of the mass of the central SMBHs.

The two simulations agree closely, and both show rapid BH growth in the halo mass range $10^{11.5}$–$10^{12.5}$ $M_\odot$ demonstrating that this rapid growth phase does not depend on the details of the SMBH feedback scheme (or indeed the SMBH seed mass, as we show in Appendix A). The origin of this transition will be investigated in Bower et al. (in preparation), showing that it emerges as a result of a change in the hot gas content of the halo (see also Bower et al. 2006). In halo masses below the transition, the gas content of galaxies is regulated by stellar feedback; however, in more massive haloes, supernova-driven outflows stall as the hot halo becomes established and the gas content of the galaxy is regulated by the more energetic SMBH driven feedback. The median $M_{\rm BH}$-M_{200} relation evolves very little with redshift, so that at $z = 2$ many massive SMBHs have already been assembled and a population of haloes with $M_{200} > 10^{12}$ $M_\odot$ already host SMBHs with $M_{\rm BH} > 10^{8.5}$ $M_\odot$. At higher redshifts the transition between the SMBH mass regimes becomes more abrupt, and SMBHs in this regime must grow rapidly as their halo mass increases which is consistent with the increasing median Eddington ratio seen in Fig. 5. SMBHs in higher-mass haloes ($>10^{12}$ $M_\odot$) have released enough energy into the host halo to ensure that the cooling time becomes long, and the galaxy is starved of further fuel for star formation. This later process results in a self-regulated growth as noted by Booth & Schaye (2010) leading, together with the BH growth due to mergers, to the small scattering well-defined slope seen in Fig. 6.

3.3 Observable diagnostics of SMBH growth

In this section we investigate observables related to gas accretion on to SMBHs. We will focus on the hard and soft X-ray AGN luminosity functions and the evolution of the space density of AGN in hard X-rays through cosmic time.

3.3.1 Hard X-ray luminosity functions

Fig. 7 shows the predicted hard (2–10 keV) X-ray luminosity function (HXRLF) over the redshift range 0–5. Intrinsic X-ray luminosities have been derived using the bolometric corrections described in Section 2.5, and include only SMBHs in the SSD regime. We show two simulations, Ref-L100N1504 (dark blue lines) and AGNdT9-L050N0752 (light blue lines). The HXRLF shows strong

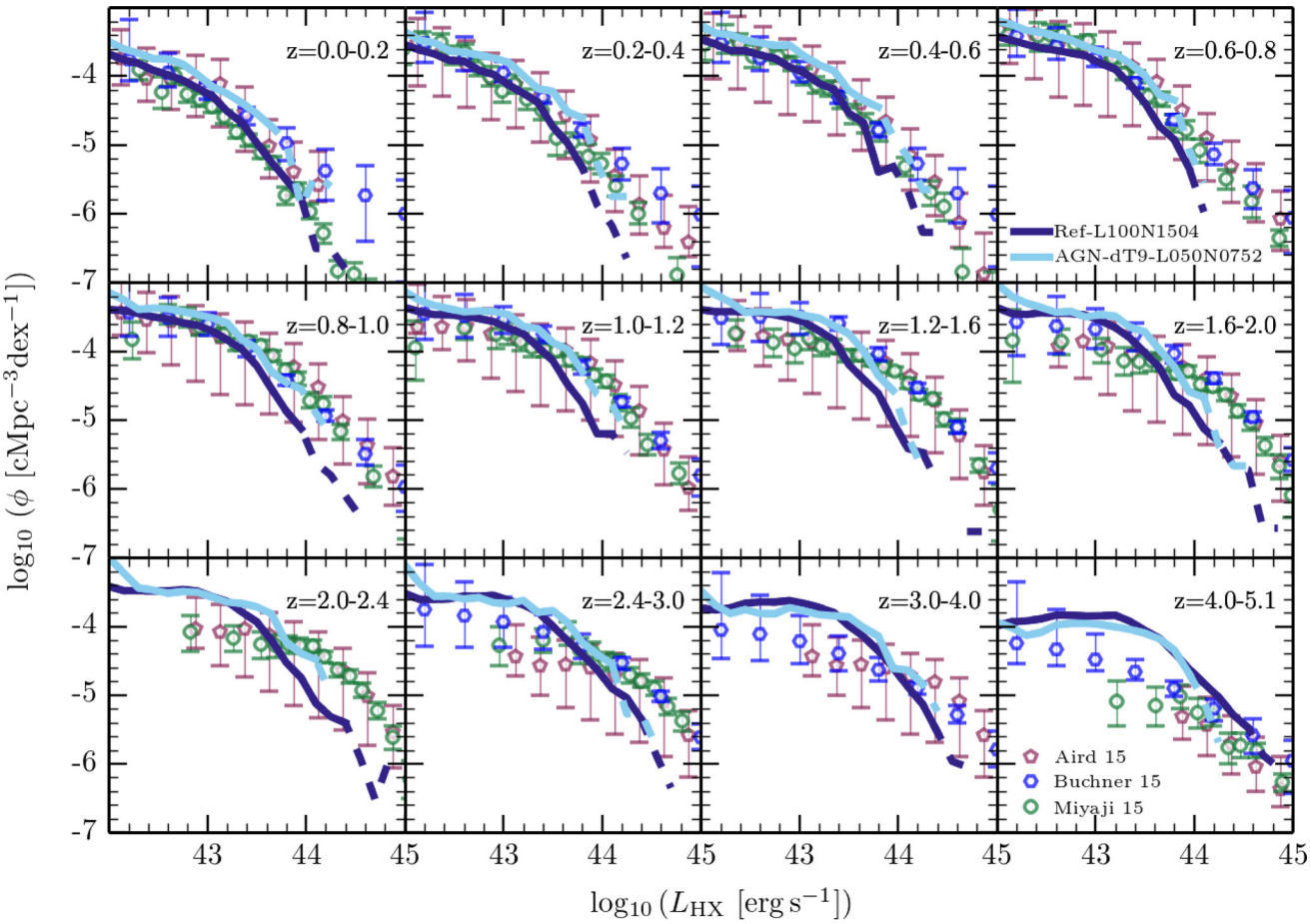

Figure 7. Evolution of the hard (2–10 keV) X-ray luminosity functions in simulations Ref-L100N1504 (dark blue) and AGNdT9-L050N0752 (light blue). Each panel corresponds to a different redshift bin as indicated. The simulation curves are dashed where there are fewer than 10 AGN per dex luminosity bin. Green circles correspond to the observational estimates from Miyaji et al. (2015), red pentagons to Aird et al. (2015) and bright blue hexagons to Buchner et al. (2015). Comparing the simulations to each other, we find good agreement at all redshifts with differences no larger than 0.2 dex in normalization. The abundance of AGN of a given luminosity increases up to $z \approx 2$ and then declines. Compared to the observations, the simulations match the data well for $z < 0.8$, but for $1.2 < z < 4.0$ they underestimate the abundance of AGN with luminosities greater than $L_{\rm HX} > 10^{44}$ erg s^{-1}, and may overestimate the abundance of fainter sources. The differences for brighter sources are, however, affected by the limited volume of our simulation.

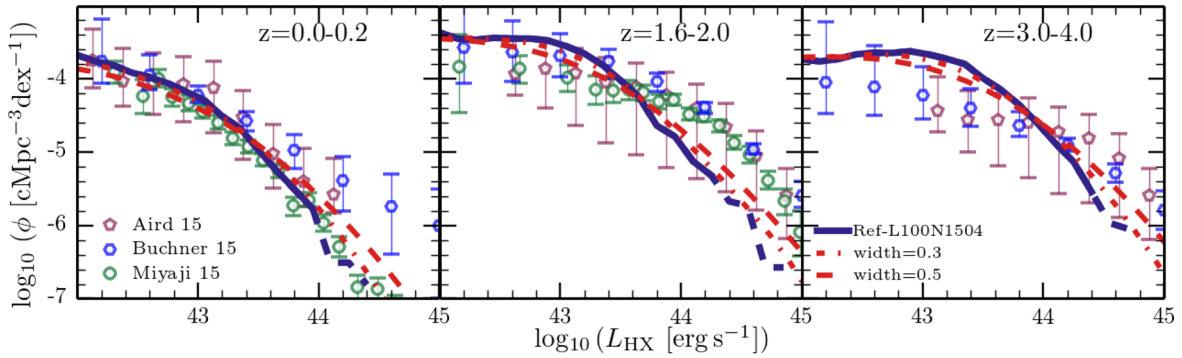

Figure 8. An illustration of the plausible impact of unresolved AGN variability on the hard X-ray luminosity function in EAGLE. Blue solid lines and points reproduce respectively model Ref-L100N1504 and observations of Fig. 7. Red dash–dotted and dashed lines represent the hard X-ray luminosity function convolved with a log-normal distribution of width 0.3 and 0.5 dex, respectively to illustrate the impact of variability not resolved by the simulations. The mean of convolution kernel is set in order to conserve the total energy released. Unresolved variability does not significantly alter the comparison between the observed luminosity function and the simulation prediction.

evolution in shape and normalization in both simulations. Below $z = 2$ the simulations agree with each other within 0.2 dex in normalization, with AGNdT9-L050N0752 slightly above the HXRLF of Ref-L100N1504. At $z > 2$ the simulations are still similar but present higher discrepancies in the bright end of the HXRLF. The bright end of the HXRLF may be affected the limited statistics available in our volume or by variability on short time-scales that is not resolved.

We also compare the predicted HXRLF to recent observational estimates based on the deep X-ray fields from Miyaji et al. (2015) (green circles), Aird et al. (2015) (red pentagons) and Buchner et al. (2015) (bright blue hexagons). Overall, the comparison between the observations and simulations is encouraging, given the simplicity of the subgrid model used. We stress that the parameters of SMBH growth and AGN feedback were calibrated to match the stellar mass function at $z = 0.1$ and the normalization of the $M_{\rm BH}$-$M_{\rm star}$ relation, not to match the evolution of AGN. Looking in detail, the observations are in good agreement (within the observational error bars) out to $z = 0.8$; however, at $1.2 < z < 4.0$ and higher luminosities ($L_{\rm HX} > 10^{44}$ erg s^{-1}), the simulation HXRLF appears to decline with $L_{\rm HX}$ more quickly than seen in the observations. The discrepancy does not appear to be due to the sampling statistics but we cannot entirely rule out the possibility that it is due to the finite volume of the simulation (see Appendix A) because we sample a relatively small number of massive galaxies in the simulations. Above $z \sim 2$, there is an overabundance of low luminosity ($L_{\rm HX} < 10^{43}$ erg s^{-1}) AGN in EAGLE. In this regime, however, the observational constraints are quite uncertain, as can be seen by comparing different observational data sets.

We have mentioned previously that one possible factor that affects the HXRLF is the variability of AGN that is not resolved in the simulation. Short time-scale variations could originate from fluctuations in accretion disc viscosity, for example. In galactic binary systems such as stellar remnant compact objects, order of magnitude variations in the accretion rate arise from the ionization instability in accretion discs, and similar instabilities may be present in SMBHs (Done, Gierliński & Kubota 2007). Such 'flickering' cannot be resolved in our simulations which only attempt to model variations in the gas supply rate on 10^2 pc scales.

An illustration of the effect of short-time-scale variability is shown in Fig. 8. Here, we show the effect of convolving source luminosities with a log-normal distribution with σ between 0.3 and 0.5 dex per luminosity.

We have chosen the log-normal distribution as a simple way to illustrate the potential impact of flickering since we are interested in the effect of order of magnitude variations in source luminosity. It is important to note that the central value of the convolution kernel has been set so that the average (expectation) luminosity is independent of σ. We have explored relatively high σ values in order to assess the maximum impact of unresolved variability in the simulation. A source with $\sigma = 0.5$ is, instantaneously, an order of magnitude brighter or fainter than the mean luminosity for 5 per cent of the time, and a factor of 3 brighter or fainter for 32 per cent of the time. Values higher than 0.5 would imply that the instantaneous $L_{\rm HX}$ is almost unrelated to the SMBH accretion rate.

Solid lines reproduce the Ref-L100N1504 simulation and observational data from Fig. 7. The effect of including unresolved variability is shown as red dot–dashed and red dashed lines in Fig. 8. As the width of the convolving Gaussian is increased intrinsically low luminosity sources scatter in the high luminosity bins, and the simulation tends to agree better with the observational data. The overall effect is relatively small, however, and does not seem able to reconcile the simulation with the observational data. The convolution has little effect on the fainter luminosities ($L_{\rm HX} < 10^{43}$ erg s^{-1}) and so cannot account for the overabundance of faint sources in the simulation at $z > 4$. We have already stressed that the observational measurements are uncertain in this regime.

Although the volume of the simulation is rather small for the characterization of extreme high redshift events, for completeness we show the predicted hard X-ray luminosity function in EAGLE at $z = 5$–11 in Fig. 9. We see that the HXRLF amplitude decreases with redshift and evolves rapidly in shape. Above $z = 8$, the simulation suffers from particularly poor sampling for AGNs with $L_{\rm HX} > 10^{43}$ erg s^{-1} (indicated by the dashed line). Comparing to observational estimates from Buchner et al. (2015), we find reasonable agreement between $z = 5.1$ and 7 over the luminosity range that we are able to probe. Observational data is not available at higher redshifts in this luminosity range, and the figure presents the model predictions.

3.3.2 *Soft X-ray luminosity function*

Soft (0.5–2 keV) X-ray measurements provide a useful complement to hard X-ray surveys. The evolution of the soft X-ray AGN luminosity function (SXRLF) has been investigated by e.g. Miyaji,

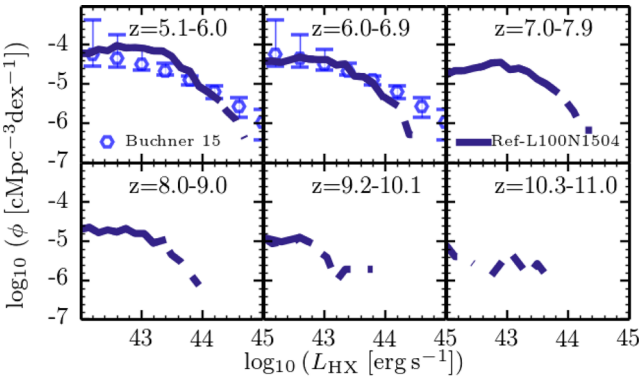

Figure 9. Hard X-ray luminosity functions of AGNs from $z = 5.1$ to $z = 11$. The HXRLF amplitude and shape evolve rapidly as redshift decreases. We compare the simulations with observations from Buchner et al. 2015 (open points with error bars), finding good agreement at $z = 5.1$ and 7 over the luminosity range that can be compared. No observational data is available at higher redshift.

Hasinger & Schmidt (2000), Hasinger, Miyaji & Schmidt (2005), Aird et al. (2015). A complication, however, is that an uncertain fraction of sources will be obscured by the gas column along the line of sight through the host galaxy to the AGN. Rather than trying to model the effects of obscuration in the simulation, we compare to the results of Aird et al. (2015) in which the effects of obscuration have been empirically corrected.

Fig. 10 shows the SXRLF for the simulation Ref-L100N1504 (solid lines). To illustrate the importance of obscuration, we have included blue dot–dashed lines to show the expected abundance of detectable (i.e. unobscured) objects using the prescription of Hasinger (2008). Comparing the SXRLF with obscuration to the one without, the fraction of obscured AGN can vary between 0.83 and 0.01 with the largest values found at low luminosities ($L_{\rm SX} < 10^{42}$ erg s^{-1}) and the smallest at high luminosities ($L_{\rm SX} > 10^{44}$ erg s^{-1}). Note, however, that these ratios are not a theoretical prediction of the simulations, but the effect of corrections derived from

We compare the predicted SXRLF (solid lines) to the observational estimates from Aird et al. (2015) (red pentagons). The observed counts are corrected for the effects of obscuration by comparing the hard- and soft-band X-ray data. The data points should therefore be compared to the solid lines derived from the simulations. The simulation broadly reproduces the observed evolution across cosmic time, particularly for the faintest part of the SXRLF ($L_{\rm SX} < 10^{42.5-44}$ erg s^{-1}) at $z < 2$. Even at low redshift, the brightest part of the SXRLF is steeper than observed, but the discrepancy is only greater than the observational uncertainties in the region where we have fewer than 10 sources per bin (shown as dashed lines).

As we discussed above, we would expect some additional contribution from unresolved variability, and we show the effect of log-normal luminosity variations between width of 0.3 and 0.5 dex as red dot–dashed and red dashed lines, respectively. As we found in Fig. 8, this has relatively little impact. Towards high redshifts ($3 < z < 4$), the simulations predict a higher amplitude of the SXRLF (particularly at luminosities of $L_{\rm SX} \sim 10^{43}$ erg s^{-1}). This might indicate an overabundance of the faint AGN in the simulations, but may also be due to a greater redshift dependence of obscuration than accounted for by Aird et al. (2015).

However, a similar over-abundance is seen in both soft and hard X-ray luminosity functions, and in general in both X-ray bands the luminosity functions follow a similar evolution. It seems therefore that the offset between the simulation and the observations must either be real (in the sense that the numerical implementation of SMBH accretion used in the simulations generates an excess of low luminosity sources) or be due to observational selection effects (for example, we have not attempted to model observational selection effects such as the difficulty of detecting faint AGN against the galaxy's nuclear star formation).

In general terms, the evolution of the SXRLF in the simulation evolves in broad agreement with the observational constraints, opening a window to explore more deeply the connection between BH accretion rates, obscuration and the gas and star formation properties of galaxies.

3.3.3 *Evolution of the comoving number density of AGN*

Fig. 11 shows the evolution of the comoving number density of AGN in the simulation Ref-L100N1504 (solid lines). As we discussed above, some AGN variability may not be accounted for in the simulation and we illustrate the effect of convolving source luminosities with a log-normal distribution of width 0.3–0.5 dex.

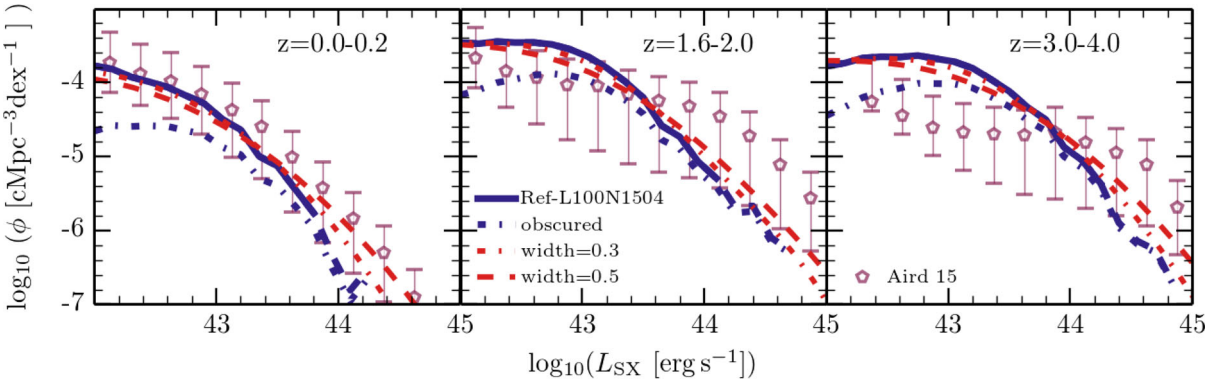

Figure 10. Evolution of the soft X-ray luminosity function. Each panel represents the SXRLF at different redshifts from $z = 0-4$ as indicated. Solid lines represent the SXRLF in the simulation Ref-L100N1504, with blue dashed lines showing the luminosity bins containing fewer than 10 AGN per dex luminosity bin. Blue dot–dashed lines represent the SXRLF when empirical obscuration estimates are applied to the simulation data. The simulation results are compared to the observational estimate of Aird et al. (2015) (red pentagons) which includes a correction for obscuration and should thus be compared to the solid lines from the simulation. Red lines represent the SXRLF convolved with log-normal luminosity variations of 0.3 (dot–dashed lines) and 0.5 (dashed lines) in dex, bringing the simulation into slightly better agreement with the observations. Discrepancies in the abundance at fainter luminosities could be the result of a more rapid evolution of the obscuration, however, similar discrepancies are seen in Fig. 7.

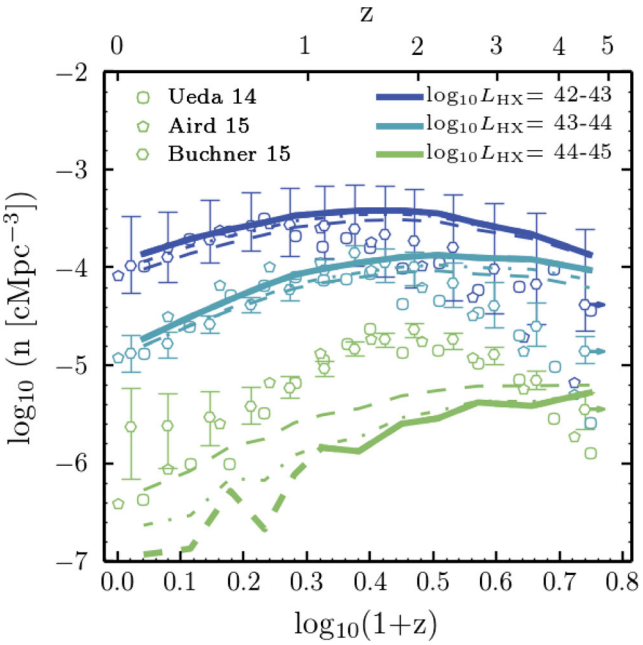

Figure 11. Evolution of the comoving number density of AGN in simulation Ref-L100N1504, broken into three different hard X-ray luminosity bins: blue solid lines correspond to AGN with $L_{\rm HX} = 10^{42-43}$ erg s^{-1}, light blue lines to AGN with $L_{\rm HX} = 10^{43-44}$ erg s^{-1} and green lines to $L_{\rm HX} = 10^{44-45}$ erg s^{-1}. The solid lines become dashed when there are less than 10 objects per dex luminosity bins. Observational estimates from Ueda et al. (2014), from Aird et al. (2015) and the values obtained by integrating the observational estimates from Buchner et al. (2015). The hexagons with arrows represent values that where estimated within a smaller redshift bin. The evolution of the comoving number density of AGN with $L_{\rm HX} = 10^{42-43}$ erg s^{-1} and $L_{\rm HX} = 10^{43-44}$ erg s^{-1} is similar to the observed estimates for $z \lesssim 1.5$ but declines more slowly with redshift than suggested by the observations at $z > 2$. The abundance of the brightest AGN is affected by the size of the simulation and additional variability not captured by the simulation. Thinner lines illustrate the effect of convolving AGN luminosities with log-normal flickering of 0.3 and 0.5 dex.

We split the AGN population into three luminosity bands as indicated in the legend. This figure reproduces the information already seen in Fig. 8, but allows us to investigate the evidence for AGN 'downsizing' more clearly. In the observational data, higher luminosity sources peak in abundance at progressively higher redshifts. A similar trend is seen in the simulations: brighter AGN ($L_{\rm HX} = 10^{44}$–10^{45} erg s^{-1}; green lines) peak at redshifts greater than 3 while fainter AGN ($L_{\rm HX} = 10^{42}$–10^{43} erg s^{-1}; dark blue lines) peak at $z \approx 1.4$.

For comparison, we show recent estimates from Ueda et al. (2014) and Aird et al. (2015). We also show values obtained by integrating the luminosity functions from Buchner et al. (2015). There is reasonable agreement between simulations and observations for the lower luminosity bins, $L_{\rm HX} = 10^{42}$–10^{43} erg s^{-1} (dark blue line) and $L_{\rm HX} = 10^{43}$–10^{44} erg s^{-1} (light blue line), out to $z \sim 1.5$. Moving towards higher redshifts, the simulations predict too many faint AGN in comparison to observations, the discrepancy becoming almost 0.8 dex in the comoving number density at $z \sim 5$. We note, however, similar discrepancies are seen in observational data due to uncertainties in detecting faint AGN at high redshifts. For example, the comoving number density of AGN of $L_{\rm HX} = 10^{42}$–10^{43} erg s^{-1} from Ueda et al. (2014) (blue circles, $10^{-4.4}$ cMpc^{-3}) is higher by 0.8 dex compared to Aird et al. (2015) (blue pentagons, $10^{-5.2}$ cMpc^{-3}) at $z \sim 5.0$. Moreover, Giallongo et al. (2015) recently reported a more abundant population of faint AGNs at $z = 4$–6 by studying AGN candidates from the multiwavelength CANDELS deep surveys (Grogin et al. 2011; Koekemoer et al. 2011). The sample was initially selected by the UV rest frame of the parent galaxy and thus is able to account for sources with marginal X-ray nuclear detections. This population might extend to even higher redshift ($z > 10$). Madau & Haardt (2015), based on this result, suggest that such contribution of active galaxies drives the reionization of hydrogen and helium satisfying several observational constrains such as the observed flatness of HI photoionization rate between $z = 2$ and $z = 5$ and the estimated integrated Thompson scattering optical depth ($\tau = 0.056$) found in the Lyman α opacity of the intergalactic medium and cosmic microwave (CMB) polarization.

The comoving number density of the brightest AGN is low in the simulations compared to the observational estimates. However, the comoving number density of the brightest AGN can be affected by additional AGN variability combined with the low numbers of bright AGN in the finite simulation volume. As we show in the figure, convolution with log-normal flickering of 0.5 dex goes some way to account for the high abundance of bright AGN seen in the observations.

Overall, while the 'downsizing' trend is present in the simulations, it is not as clear as suggested by the observational data. In particular, the abundance of AGN of a particular luminosity has a broader plateau than suggested by observations, principally because the rapid decline observed in the abundance of faint AGN at high redshift seen in observations is shallower in the simulations. At almost all redshifts, however, the simulations tend to underpredict the abundance of the brightest AGN, and their peak of their abundance occurs at too high redshift. We should be careful not to over-interpret this apparent discrepancy, however, since the abundance of these objects is poorly sampled in the simulation volume.

4 CONCLUSIONS

We have examined the evolution of supermassive black holes (SMBHs) across cosmic time predicted by the EAGLE simulations (S15, C15). The EAGLE project consists of a suite of hydrodynamical simulations with state-of-the-art subgrid models of galaxy formation including radiative cooling, star formation, reionization, abundance evolution, stellar evolution and mass-loss, feedback from star formation, and SMBH growth and AGN feedback. The parameters of these subgrid models were calibrated to reproduce the observed galaxy mass function and sizes at $z = 0.1$. In particular, the efficiency of AGN accretion and feedback were set to reproduce the break in the stellar mass function at $z = 0.1$ and the normalization of the SMBH mass-stellar mass relation at $z = 0$. It is important to emphasize that the subgrid models of SMBH growth and AGN feedback do not make any explicit distinction between *quasar* and *radio* modes, and that we only distinguish sources with high and low Eddington ratios during the analysis. The main findings are summarized as follows:

(i) The main properties of nearby SMBHs are reproduced well in the EAGLE simulations. Within the observational uncertainties, the $z = 0$ SMBH mass function is similar to estimates from Shankar et al. (2004), Marconi et al. (2004) and Shankar (2013), and the density of SMBHs in the local Universe is also comparable to that observed. This agreement is partly the result of the calibration strategy (see Fig. 1). As a post-processing step, we divide the present-day black hole mass function as a function of Eddington ratio, $\lambda_{\rm Edd}$. We associate sources with $\lambda_{\rm Edd} \geq 10^{-2}$ with X-ray

luminous *Shakura–Sunyaev discs* (SSDs), sources with $10^{-4} \leq \lambda_{\rm Edd} < 10^{-2}$ as *Advection Dominated Accretion Flows* (ADAFs) and classify that sources with $\lambda_{\rm Edd} < 10^{-4}$ as inactive. At low redshift the mass function is dominated by inactive and ADAF black holes (Fig. 2). Assuming that SMBHs cycle between the SSD, ADAF and inactive states, we estimate that the *duty cycle* for SMBHs in the SSD state is ∼0.01, which is comparable to the observational estimates (e.g. Soltan 1982; Yu & Tremaine 2002; Marconi et al. 2004).

(ii) The mass function of SMBHs in the EAGLE simulation evolves rapidly in amplitude from $z > 5$ to $z = 2$. At redshift 2 a large fraction of the $M_{\rm BH} > 10^7\,{\rm M}_\odot$ population has already been formed (Fig. 3). Between $z = 2$ and the present-day the mass function evolves more gradually in normalization. When we break this evolution down by accretion state, we find that luminous SSD systems, while a minor contribution at the present-day, become increasingly dominant at high redshift (Fig. 4). This trend can also be clearly seen by examining the evolution of the Eddington ratio distribution directly (Fig. 5).

(iii) We examine the dependence of black hole mass on the dark matter halo mass, M_{200} (Fig. 6). The $M_{\rm BH}$–M_{200} relation has a characteristic shape, with SMBH masses growing little above the seed mass in haloes less massive than $\sim 10^{12}\,{\rm M}_\odot$, but showing a sharp rise in more massive haloes. The fast growth of the SMBH ends when its mass exceeds $M_{\rm BH} \sim 10^8\,{\rm M}_\odot$. SMBHs follow an almost linear trend with M_{200} in larger haloes. The characteristic shape of this relation evolves little with redshift, with a suggestion that the steep rise in mass becomes more abrupt as redshift increases.

(iv) The black hole mass function, the Eddington ratio distribution and the SMBH dependence on halo mass cannot be directly observed and must be inferred by combining observational surveys with, for example, a calibration between black hole mass and stellar mass. To facilitate a more direct comparison between the model and observational data, we compute the X-ray luminosity function in the rest frame for SMBHs in the SSD state. We use bolometric corrections from Marconi et al. (2004) to convert the bolometric output predicted by the model into the intrinsic hard and soft X-ray luminosities. We compare the hard-band X-ray luminosity functions with the observational measurements from Miyaji et al. (2015), Aird et al. (2015) and Buchner et al. (2015) (Fig. 7). The finite volume of the simulation limits the comparison to hard X-ray AGN luminosities lower than $L_{\rm HX} \sim 10^{44}\,{\rm erg\,s^{-1}}$. At low redshifts, the simulations agree extremely well with the observational data. At higher redshift ($z > 1$) the simulations tend to underpredict the abundance of high luminosity sources with $L_{\rm HX} \gtrsim 10^{44}\,{\rm erg\,s^{-1}}$, although we cannot rule out the possibility that this is a result of the simulation's limited volume. At $z = 2$ and above, the amplitude of the predicted luminosity function appears higher than observed, particularly around $L_{\rm HX} \sim 10^{43}\,{\rm erg\,s^{-1}}$, although some caution is required since we have not attempted to include observational selection effects (other than bolometric corrections) in our predictions. We find a similar result when we compare to obscuration-corrected soft-band X-ray luminosity functions from Aird et al. (2015).

(v) The hard X-ray luminosity functions we derive include the effect of variability captured by the model due to gas flows on kpc scales, but unresolved variability (for example due to flickering in the accretion disc) that may cause additional fluctuations in luminosity. Given the steepness of the X-ray luminosity function, this could have an important impact. However, we present a simple model based on additional log-normal distributed flickering to show that this has only a limited impact on the comparison with observational data (Fig. 8).

(vi) We investigate AGN *downsizing* in the simulation (Fig. 11). The observed trend seen in observational data is qualitatively reproduced: the comoving number density of higher luminosity AGN peaks at higher redshift, and the simulations are in good quantitative agreement with the observational data for $L_{\rm HX} < 10^{44}\,{\rm erg\,s^{-1}}$ at $z \lesssim 2$. At higher redshifts, the simulations produce more active SMBHs than observed, resulting in a shallower roll-over of the AGN abundance. The finite volume of the simulations and the possible effects of flickering make difficult to reliably compare the abundance of the more luminous AGN. Taken at face value, the simulations do not predict the rapid rise in the abundance of the brightest ($L_{\rm HX} > 10^{44}\,{\rm erg\,s^{-1}}$) objects seen in some observational surveys between $z = 0$ and $z = 2$. Larger volume simulations, and a better understood model for AGN flickering, are required to determine if this is due to a real discrepancy between the hydrodynamical model and the observational data.

The results we find are broadly consistent with other simulations and semi-analytic calculations. For example, Fanidakis et al. (2012) used a version of the semi-analytic GALFORM code, similar to that of Bower et al. (2006), in which galaxy formation is approximated as a network of analytic differential equations that are applied to haloes that grow in a dark matter *N*-body simulation. It is assumed that SMBHs grow either by accretion from the diffuse gas halo, if this is stable against cooling, or as a result of gas flows produced during merger and disc instability driven starbursts. The semi-analytic model is able to probe large volumes and hence more luminous sources, and the model indeed generates a population of very luminous sources at high redshift, improving the match to the observational data. Similarly to EAGLE, theses calculations do not show the strong 'down-sizing' trend inferred from the observational data and the authors conclude that the perceived evolution is largely the result of obscuration.

Recently, Hirschmann et al. (2014) and Sijacki et al. (2015) have presented an analysis of black hole properties in large volume cosmological simulations. Hirschmann et al. (2014) combined simulations of a 500 Mpc region at low resolution (a factor of ∼100 higher than the particle mass of the Ref-L100N1504 simulation) run to $z = 0$, with the results obtained from a 68 Mpc region with a resolution similar to that of the EAGLE simulation, but run only to $z = 1$. Their prescription of AGN feedback is extensively based on Springel et al. (2005) and two explicit modes of AGN feedback are assumed, namely, a quasar and a radio mode with a switchover depending on the source Eddington ratio. The efficiency of feedback in radio mode is 4 times larger than that in quasar mode. These models generally fit the observed AGN luminosity functions reasonably well, although they also find that the abundance of $L_{\rm HX} \sim 10^{43}\,{\rm erg\,s^{-1}}$ sources tends to be overestimated when the resolution of their large volume calculation is increased. Accounting for the differences in resolution and volume, their results appear compatible with our own.

Sijacki et al. (2015) presented an analysis of SMBHs in the Illustris simulation (Vogelsberger et al. 2014) which, while similar in volume and resolution of our work, differs greatly in its implementation of AGN feedback and accretion on to SMBHs. In particular, the Illustris simulation employs different schemes for feedback in high and low Eddington ratio sources. In low accretion states radio feedback is implemented by depositing energy in thermal 'bubbles' at some distance from the central galaxy (Sijacki et al. 2007). In this high accretion mode feedback energy is dumped at the location of the BH at every timestep, a procedure that is expected to result in significant radiative losses at this resolution (e.g. Dalla Vecchia

& Schaye 2012) The black hole mass function derived from the Illustris simulations differs significantly in shape from that in EAGLE, being essentially a power law that increases in steepness as a function of mass. At low redshift, rare SMBHs (more massive than $M_{\rm BH} \sim 10^9\,{\rm M}_\odot$) are more abundant, but most of these SMBHs accrete at rates less than 10^{-4} of the Eddington limit. The results for the luminosity functions are broadly similar to ours (within the uncertainty of the data that are shown). In particular, they also find that the model tends to overpredict the abundance of moderate luminosity ($L_{\rm HX} \sim 10^{43}\,{\rm erg\,s^{-1}}$) AGN at $z > 2$. In terms of AGN downsizing, the model does appear to capture the rapid decline of the abundance of high-luminosity sources, although it is unclear whether this is largely affected by the selection of sources based on an Eddington ratio criterion of $\lambda_{\rm Edd} > 10^{-4}$, given the significant difference in the black hole mass functions of the simulations.

Although most of our qualitative results seem compatible with these earlier works. It is important to stress the greater simplicity of the AGN feedback model used in EAGLE, and the fact that basic galaxy properties like stellar masses and sizes are better reproduced. It is therefore encouraging that the model, which uses a single mode of AGN feedback and in which AGN feedback energy is a fixed fraction of the accretion rate, captures so many of the trends seen in observational data. The results we have presented from the EAGLE simulations open a new window to investigate the co-evolution of the SMBH growth and galaxy evolution. In future work, we will investigate more consistently the obscuration of AGN due to gas and dust by including the properties of the host galaxy. We will also investigate the effects of AGN feedback on the host galaxies and how this evolves through cosmic time.

ACKNOWLEDGEMENTS

We thank Johannes Buchner, James Aird, Francesco Shankar and Takamitsu Miyaji for providing their observational data and the referee for the useful comments. This work would have not be possible without Lydia Heck's technical support. YRG thanks Johannes Buchner for his useful comments about observations. YRG gratefully acknowledges financial support from the Mexican Council for Science and Technology (CONACYT) (Studentship No. 213183) and partial support from Center of Excellence in Astrophysics and Associated Technologies (PFB 06). This work used the DiRAC Data Centric system at Durham University, operated by the Institute for Computational Cosmology on behalf of the STFC DiRAC HPC Facility (www.dirac.ac.uk). This equipment was funded by BIS National E-infrastructure capital grant ST/K00042X/1, STFC capital grant ST/L00075X/1, and STFC DiRAC Operations grant ST/K003267/1 and Durham University. DiRAC is part of the National E-Infrastructure. We also gratefully acknowledge PRACE for awarding us access to the resource Curie based in France at Tres Grand Centre de Calcul. This work was sponsored by the Dutch National Computing Facilities Foundation (NCF) for the use of supercomputer facilities, with Financial support from the Netherlands Organization for Scientific Research (NWO). The research was supported in part by the European Research Council under the European Union's Seventh Framework Programme (FP7/2007-2013)/ERC Grant agreements 278594-GasAroundGalaxies, GA 267291 Cosmiway, and 321334 dustygal, the Interuniversity Attraction Poles Programme initiated by the Belgian Science Policy OWNce ([AP P7/08 CHARM]), the National Science Foundation under Grant No. NSF PHY11-25915, the UK Science and Technology Facilities Council (grant numbers ST/F001166/1 and ST/I000976/1. We thank contributors to SciPy,[2] Matplotlib,[3] and the PYTHON programming language.[4]

CDV acknowledges financial support from the Spanish Ministry of Economy and Competitiveness (MINECO) under the Severo Ochoa Programs SEV-2011-0187 and SEV-2015-0548 and through grants AYA2013-46886 and AYA2014-58308.

REFERENCES

Abramowicz M. A., Chen X., Taam R. E., 1995, ApJ, 452, 379
Aird J. et al., 2010, MNRAS, 401, 2531
Aird J., Coil A. L., Georgakakis A., Nandra K., Barro G., Perez-Gonzalez P. G., 2015, MNRAS, 451, 1892
Anglés-Alcázar D., Davé R., Faucher-Giguère C.-A., Özel F., Hopkins P. F, 2016, preprint (arXiv:1603.08007)
Bahé Y. M. et al., 2016, MNRAS, 456, 1115
Bandara K., Crampton D., Simard L., 2009, ApJ, 704, 1135
Binney J., Tabor G., 1995, MNRAS, 276, 663
Bondi H., Hoyle F., 1944, MNRAS, 104, 273
Booth C. M., Schaye J., 2009, MNRAS, 398, 53
Booth C. M., Schaye J., 2010, MNRAS, 405, L1
Bower R. G., Benson A. J., Malbon R., Helly J. C., Frenk C. S., Baugh C. M., Cole S., Lacey C. G., 2006, MNRAS, 370, 645
Buchner J. et al., 2015, ApJ, 802, 89
Chabrier G., 2003, PASP, 115, 763
Choi E., Naab T., Ostriker J. P., Johansson P. H., Moster B. P., 2014, MNRAS, 442, 440
Churazov E., Brüggen M., Kaiser C. R., Böhringer H., Forman W., 2001, ApJ, 554, 261
Crain R. A. et al., 2009, MNRAS, 399, 1773
Crain R. A. et al., 2015, MNRAS, 450, 1937 (C15)
Croton D. J. et al., 2006, MNRAS, 365, 11
Dalla Vecchia C., Schaye J., 2012, MNRAS, 426, 140
De Lucia G., Blaizot J., 2007, MNRAS, 375, 2
Done C., Gierliński M., Kubota A., 2007, A&AR, 15, 1
Fanidakis N. et al., 2012, MNRAS, 419, 2797
Ferland G. J. et al., 2013, Rev. Mex. Soc., 49, 1
Furlong M. et al., 2015a, MNRAS, 450, 4486
Furlong M. et al., 2015b, preprint (arXiv:1510.05645)
Giallongo E. et al., 2015, A&A, 578, A83
Graham A. W., 2016, Galactic Bulges, 418, 263
Grogin N. A. et al., 2011, ApJS, 197, 37
Haardt F., Madau P., 2001, in Neumann D. M., Van J. T. T., eds, XXIst Moriond Astrophysics Meeting, Clusters of Galaxies and the High Redshift Universe Observed in X-rays
Hasinger G., 2008, A&A, 490, 905
Hasinger G., Miyaji T., Schmidt M., 2005, A&A, 441, 417
Hirschmann M., Somerville R. S., Naab T., Burkert A., 2012, MNRAS, 426, 237
Hirschmann M., Dolag K., Saro A., Bachmann L., Borgani S., Burkert A., 2014, MNRAS, 442, 2304
Hopkins P. F., Richards G. T., Hernquist L., 2007, ApJ, 654, 731
Hopkins P. F., Hernquist L., Cox T. J., Keres D., Wuyts S., 2009, ApJ, 691, 1424
Jenkins A., 2010, MNRAS, 403, 1859
Jenkins A., 2013, MNRAS, 434, 2094
Kelly B. C., Shen Y., 2013, ApJ, 764, 45
Kennicutt R. C., Jr, 1998, ARA&A, 36, 189
Khandai N., Di Matteo T., Croft R., Wilkins S. M., Feng Y., Tucker E., DeGraf C., Liu M.-S., 2015, MNRAS, 450, 1349
Koekemoer A. M. et al., 2011, ApJS, 197, 36
Kormendy J., Ho L. C., 2013, ARA&A, 51, 511

[2] http://www.scipy.org
[3] http://www.matplotlib.sourceforge.net
[4] http://www.python.org

Lagos C. d. P. et al., 2015, MNRAS, 452, 3815
Lansbury G. B. et al., 2015, ApJ, 809, 115
Lewis A., Challinor A., Lasenby A., 2000, ApJ, 538, 473
Lusso E. et al., 2012, MNRAS, 425, 623
McAlpine S. et al., 2016, Astron. Comput., 15, 72
McCarthy I. G., Schaye J., Ponman T. J., Bower R. G., Booth C. M., Dalla Vecchia C., Crain R. A., Springel V., 2010, MNRAS, 406, 822
McConnell N. J., Ma C.-P., 2013, ApJ, 764, 184
Madau P., Haardt F., 2015, ApJ, 813, L8
Marconi A., Risaliti G., Gilli R., Hunt L. K., Maiolino R., Salvati M., 2004, MNRAS, 351, 169
Miyaji T., Hasinger G., Schmidt M., 2000, A&A, 353, 25
Miyaji T. et al., 2015, ApJ, 804, 104
Narayan R., Yi I., 1994, ApJ, 428, L13
Planck Collaboration I et al., 2014, A&A, 571, A1
Power C., Nayakshin S., King A., 2011, MNRAS, 412, 269
Rees M. J., Begelman M. C., Blandford R. D., Phinney E. S., 1982, Nature, 295, 17
Rosas-Guevara Y. M. et al., 2015, MNRAS, 454, 1038
Schaller M., Dalla Vecchia C., Schaye J., Bower R. G., Theuns T., Crain R. A., Furlong M., McCarthy I. G., 2015, MNRAS, 454, 2277
Schaye J., 2004, ApJ, 609, 667
Schaye J., Dalla Vechia C., 2008, MNRAS, 383, 1210
Schaye J. et al., 2010, MNRAS, 402, 1536
Schaye J. et al., 2015, MNRAS, 446, 521 (S15)
Schmidt M., 1959, ApJ, 129, 243
Shakura N.I., Syunyaev R. A., 1973, A&A, 24, 337
Shankar F., 2013, Class. Quantum Gravity, 30, 244001
Shankar F., Salucci P., Granato G. L., De Zotti G., Danese L., 2004, MNRAS, 354, 1020
Sijacki D., Springel V., Di Matteo T., Hernquist L., 2007 MNRAS, 380, 877
Sijacki D., Vogelsberger M., Genel S., Springel V., Torrey P., Snyder G. F., Nelson D., Hernquist L., 2015, MNRAS, 452, 575
Soltan A., 1982, MNRAS, 200, 115
Springel V., 2005, MNRAS, 364, 1105
Springel V., Di Matteo T., Hernquist L., 2005, MNRAS, 361, 776
Steffen A. T., Barger A. J., Cowie L. L., Mushotzky R. F., Yang Y., 2003, ApJ, 596, L23
Trayford J. W., Theuns T., Bower R. G., Crain R. A., Lagos C. del P., Schaller M., Schaye J., 2016, MNRAS, 460, 3925
Treister E., Urry C. M., Virani S., 2009, ApJ, 696, 110
Ueda Y., Akiyama M., Ohta K., Miyaji T., 2003, ApJ, 598, 886
Ueda Y., Akiyama M., Hasinger G., Miyaji T., Watson M. G., 2014, ApJ, 786, 104
Vasudevan R. V., Fabian A. C., 2009, MNRAS, 392, 1124
Vogelsberger M. et al., 2014, MNRAS, 444, 1518
Wiersma R. P. C., Schaye J., Theuns T., Smith B. D., 2009a, MNRAS, 393, 99
Wiersma R. P. C., Schaye J., Theuns T., Dalla Vecchia C., Tornatore L., 2009b, MNRAS, 399, 574
Yu Q., Tremaine S., 2002, MNRAS, 335, 965

APPENDIX A: CONVERGENCE TESTS

Following the discussion of the numerical convergence in S15, we use this appendix to investigate the impact of the simulation volume on AGN observables. We also present the effects of varying the initial seed SMBH mass and simulation resolution on the AGN luminosity functions. The simulations that we consider are described in Table A1 and Table 1.

Fig. A1 investigates the sensitivity to the volume of the simulation of the hard X-ray luminosity function (HXRLF) at $z = 1$, the median of the $z = 0$ SMBH mass-halo mass relation and the SMBH mass function at $z = 0$. Dash lines show the limit of our sampling statistics. The left-hand panel of Fig. A1 shows a good convergence in the HXRLF. The discrepancies for the HXRLF are smaller than 0.2 dex between simulations in the brightest part of the HXRLF. The plots in the figure also show excellent agreement within these limitations.

Fig. A2 shows the same panels, but compares the simulations Ref-L100N1504 (blue), Small-seeds-L050N0752 (pink) and Recal-L025N0752 (green). Although we compare different box sizes, the previous figures show that this is not a concern providing that the sampling statistics are appropriately accounted for. The left-hand panel shows that the HXRLF is insensitive to resolution and to a change in the model for AGN feedback. Decreasing the SMBH seed mass by an order of magnitude has only a small effect (compared to observational uncertainties) at the faintest luminosities shown. The middle panel of Fig. A2 shows the median of the distribution of the $M_{\rm BH}$-M_{200} relation at $z = 0$. The median and scatter of each simulation shows a similar shape, however, the simulation Small-seeds-L050N0752 presents a sharper rise in haloes of $10^{11.5-12.5}\,{\rm M}_{\odot}$ in comparison to the other simulations. This results from the SMBHs in Small-seeds-L050N0752 having to grow faster to reach the self-regulated $M_{\rm BH}$-M_{200} relation. Note however, that this steep rise persists in the three simulations, indicating that this fast growth of SMBHs in such haloes are independent of the subgrid parameters of the simulation. The right-hand panel presents the SMBH mass function at $z = 0$ in simulations Ref-L100N1504, Small-seeds-L050N0752 and Recal-L025N0752. The agreement between Ref-L100N1504 and Recal-L025N0752 is better than 0.2 dex, comparable to the differences in the galaxy mass functions of these simulations. In contrast, the lower mass end of the SMBH mass function($M_{\rm BH} < 10^{7.5}\,{\rm M}_{\odot}$) is strongly affected by the SMBH seed mass. The simulation Small-seeds-L050N0752 predicts lower values for the SMBH mass function by $\sim$1 dex for SMBHs with mass smaller than $10^{7}\,{\rm M}_{\odot}$. Nevertheless, the massive end of the SMBH mass function present an impressive level of agreement between simulations.

APPENDIX B: CHOICE OF ACCRETION REGIMES

In Section 2.4, we define two active accretion regimes that depend on the value of Eddington ratio. We assume that black holes with $\lambda_{\rm Edd}$ that are higher than 10^{-2} are luminous sources of X-rays (since the nuclear disc is thin and radiative cooling efficient) and consider them

Table A1. Box length, initial particle number, initial baryonic and dark matter particle mass, comoving and maximum proper gravitational softening for the EAGLE simulations used in this paper.

Name	L [cMpc]	N	$m_{\rm g}$ [$\,{\rm M}_{\odot}$]	$m_{\rm DM}$ [$\,{\rm M}_{\odot}$]	$\epsilon_{\rm com}$ [ckpc]	$\epsilon_{\rm prop}$ [ckpc]
Ref-L100N1504	100	2×1504^3	1.81×10^6	9.70×10^6	2.66	0.70
Ref-L050N0752	50	2×752^3	1.81×10^6	9.70×10^6	2.66	0.70
Small-seeds-L050N0752	50	2×752^3	1.81×10^6	9.70×10^6	2.66	0.70
Ref-L025N0376	25	2×376^3	1.81×10^6	9.70×10^6	2.66	0.70
Recal-L025N0752	25	2×752^3	2.26×10^5	1.21×10^6	1.33	0.35

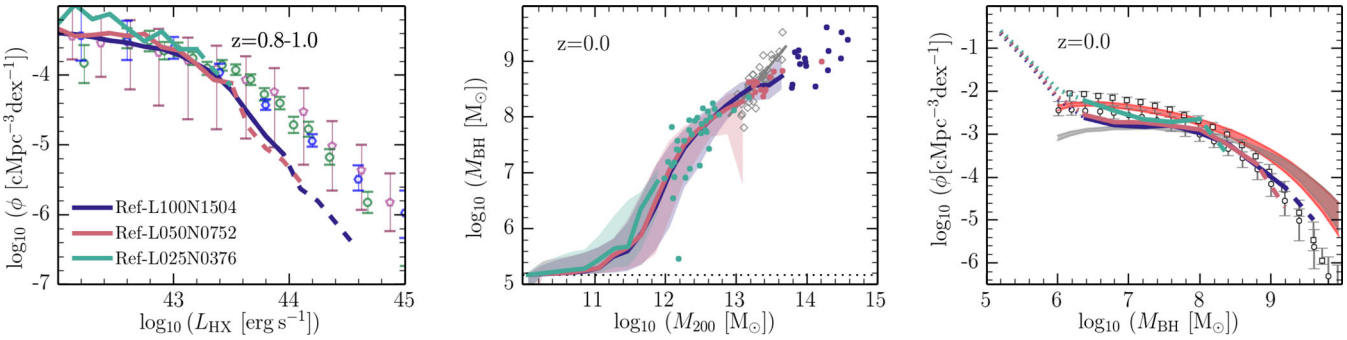

Figure A1. Convergence by box size. Left-hand panel: the HXRLF at $z = 0.8$–1.0 in the simulations Ref-L100N1504 (blue), Ref-L050N0752 (pink) and Ref-L025N0376 (green). The discrepancies between simulations Ref-L100N1504 and Ref-L050N0752 are smaller than 0.2 dex for $L_{\rm HX} < 10^{44}$ erg s^{-1}. Middle panel: the median of the $M_{\rm BH}$-M_{200} relation at $z = 0$, with shaded regions showing the 10th and 90th percentiles of the distribution. In each panel, observational data is presented following Figs 1, 5 and 7. Right-hand panel: the SMBH mass function at $z = 0$. There is good consistency between results in different simulation volumes.

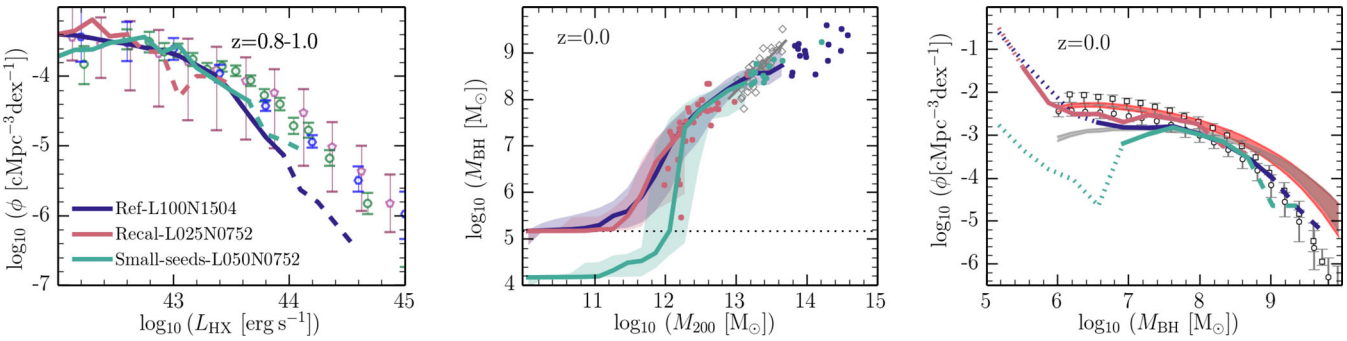

Figure A2. Similar to Fig. A1 but showing the simulations Ref-L100N1504 (blue), Recal-L025N0752 (pink) and Small-seeds-L050N0752 (green). The panels investigate the dependence on resolution and on the assumed SMBH seed mass. The $M_{\rm BH}$-M_{200} distribution presents a steep rise in haloes with $M_{200} \sim 10^{11.5-12.5}$ M$_\odot$ in all simulations, but is sharper in Small-seeds-L050N0752, while the SMBH mass function and HXRLF are largely unaffected.

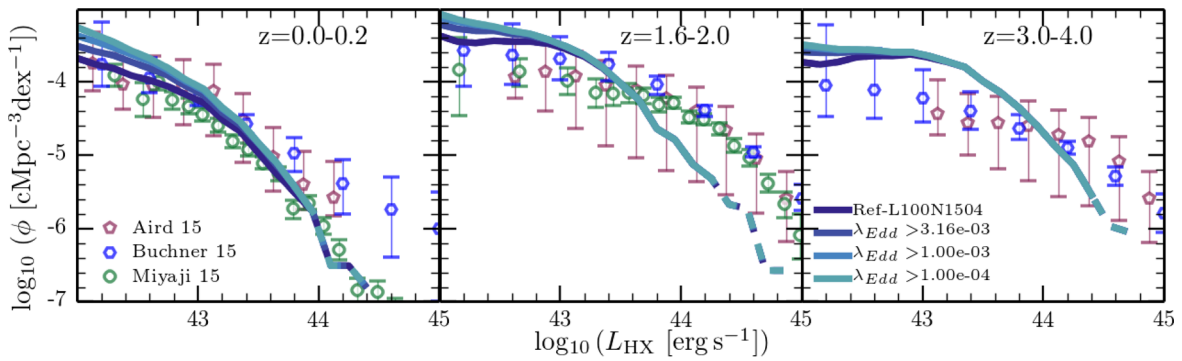

Figure B1. Similar to Fig. 8 but showing the simulation Ref-L100N1504 (blue) with increasing value of $\lambda_{\rm Edd}$ of SMBHs to be consired SSDs. Different colours indicate different value of $\lambda_{\rm Edd}$ as indicate the legend. SMBHs above of this limit are considered in the HXRLF. The HXRLF are largely unaffected by this limit, specially the bright end of the HXRLF.

as SSDs. Lower luminosity sources are assumed not to contribute to the X-ray luminosity functions we show in the main text. In this appendix, we explore the impact of varying this limit. Fig. B1 shows the HXRLF considering SMBH to be X-ray luminous when $\lambda_{\rm Edd}$ is larger than a minimum that varies from 10^{-4} to 10^{-2}. We show redshifts from $z = 0$ to $z = 4$. The dependence is weak, especially for the bright end of HXRLF. For the faint end of the HXRLF, (AGN with $L_{\rm HX}$ lower than 10^{43} erg s^{-1}) the difference becomes of ∼0.5 dex, comparing $\lambda_{\rm Edd} > 10^{-2}$ and $\lambda_{\rm Edd} > 10^{-4}$. This discrepancy becomes smaller with increasing redshift and is smaller than the observational error bars.

This paper has been typeset from a TEX/LATEX file prepared by the author.